Geoscience Frontiers 6 (2015) 373–387

HOSTED BY

Contents lists available at ScienceDirect

China University of Geosciences (Beijing)

Geoscience Frontiers

journal homepage: www.elsevier.com/locate/gsf

Focus paper

Prograde and retrograde growth of monazite in migmatites: An example from the Nagercoil Block, southern India

Tim E. Johnson [a,*], Chris Clark [a], Richard J.M. Taylor [a], M. Santosh [b], Alan S. Collins [c]

[a] Department of Applied Geology, The Institute for Geoscience Research (TIGeR), Curtin University, GPO Box U1987, Perth, WA 6845, Australia
[b] School of the Earth Sciences and Resources, China University of Geosciences (Beijing), 29 Xueyuan Road, Beijing 100083, China
[c] Tectonics, Resources and Exploration (TRaX), Department of Earth Sciences, University of Adelaide, SA 5005, Australia

ARTICLE INFO

Article history:
Received 29 October 2014
Received in revised form
3 December 2014
Accepted 6 December 2014
Available online 27 December 2014

Keywords:
Monazite
Migmatite
Zircon
Geochronology
Phase equilibria modelling
Gondwana

ABSTRACT

Data from a migmatised metapelite raft enclosed within charnockite provide quantitative constraints on the pressure–temperature–time (P–T–t) evolution of the Nagercoil Block at the southernmost tip of peninsular India. An inferred peak metamorphic assemblage of garnet, K-feldspar, sillimanite, plagioclase, magnetite, ilmenite, spinel and melt is consistent with peak metamorphic pressures of 6–8 kbar and temperatures in excess of 900 °C. Subsequent growth of cordierite and biotite record high-temperature retrograde decompression to around 5 kbar and 800 °C. SHRIMP U–Pb dating of magmatic zircon cores suggests that the sedimentary protoliths were in part derived from felsic igneous rocks with Palaeoproterozoic crystallisation ages. New growth of metamorphic zircon on the rims of detrital grains constrains the onset of melt crystallisation, and the minimum age of the metamorphic peak, to around 560 Ma. The data suggest two stages of monazite growth. The first generation of REE-enriched monazite grew during partial melting along the prograde path at around 570 Ma via the incongruent breakdown of apatite. Relatively REE-depleted rims, which have a pronounced negative europium anomaly, grew during melt crystallisation along the retrograde path at around 535 Ma. Our data show the rocks remained at suprasolidus temperatures for at least 35 million years and probably much longer, supporting a long-lived high-grade metamorphic history. The metamorphic conditions, timing and duration of the implied clockwise P–T–t path are similar to that previously established for other regions in peninsular India during the Ediacaran to Cambrian assembly of that part of the Gondwanan supercontinent.

1. Introduction

The Neoproterozoic era was a dynamic period in Earth history that witnessed the breakup of the supercontinent Rodinia and the assembly of its successor, Gondwana (Meert, 2003; Boger and Miller, 2004; Collins and Pisarevsky, 2005; Meert and Lieberman, 2008; Nance et al., 2014). The amalgamation of Gondwana occurred through collision of numerous continental blocks to produce some of the most extensive mountain ranges ever built on Earth (Kröner, 1984; Trompette, 1997). The eroded remnants of these orogenic belts expose highly deformed and metamorphosed rocks that permit investigation of the deep crustal processes occurring during supercontinent formation.

Constraining the pressure–temperature–time (P–T–t) evolution of metamorphic rocks is key to unravelling the geodynamic processes involved in their formation (e.g. Brown, 2014). Quantitative information on the P–T conditions of peak and retrograde metamorphism, as well as semi-quantitative constraints on the prograde evolution, is derived via forward modelling of phase equilibria that may be applied to a wide range of common crustal protoliths metamorphosed in a variety of tectonothermal environments under both subsolidus and suprasolidus conditions (e.g. White et al., 2001, 2007; Johnson and Brown, 2004; Evans and Bickle, 2005; Diener et al., 2008; Johnson et al., 2008, 2010, 2014; Rebay et al., 2010; Johnson and White, 2011; Korhonen et al., 2013, 2014). Quantitative constraints on the timing and duration of crustal metamorphism most commonly use U–Pb dating of accessory minerals, in particular zircon and monazite that occur in

* Corresponding author. Present address: Department of Applied Geology, Curtin University, GPO Box U1987, Perth, WA 6845, Australia. Tel.: +61 8 92667332; fax: +61 8 92663153.
E-mail address: tim.johnson@curtin.edu.au (T.E. Johnson).
Peer-review under responsibility of China University of Geosciences (Beijing)

http://dx.doi.org/10.1016/j.gsf.2014.12.003

almost all intermediate to felsic (meta) igneous rocks and siliciclastic (meta) sediments. Increasingly, age data from accessory minerals are used in conjunction with their trace element compositions to place temporal constraints on the timing of formation or consumption of particular phases, including melt, to constrain segments of a metamorphic *P–T–t* path (Rubatto, 2002; Hermann and Rubatto, 2003; Rubatto et al., 2006; Harley et al., 2007; Clark et al., 2009a; Buick et al., 2010; Taylor et al., 2015).

In migmatites and residual granulites, which represent the most abundant components of the lower crust, new metamorphic growth of zircon and monazite is generally assumed to occur due to saturation of zirconium and light rare earth elements (LREE) in the melt as it cools and crystallises, and the corresponding age data to date high-temperature retrogression (Kelsey et al., 2008; Kelsey and Powell, 2011; Yakymchuk and Brown, 2014). In the case of zircon, the Zr required for new growth is supplied to the melt by dissolution of pre-existing magmatic (in the case of igneous protoliths) or detrital (in the case of metasedimentary rocks) zircon, which later precipitates as the SiO_2-saturated melt cools and attains Zr saturation. However, monazite requires a source of phosphorus as well as LREE. Thus, monazite may form from the prograde breakdown of pre-existing phosphates, notably apatite, which is a common stable mineral at lower (subsolidus) metamorphic grades but which may break down incongruently as the rocks begin to melt (Wolf and London, 1994, 1995).

Here we combine field and petrographic observations, phase equilibria modelling and *in situ* U–Pb geochronology of zircon and monazite coupled with trace element analysis of these accessory phases and garnet from a sample of aluminous metapelite. We use these data to provide quantitative constraints on the pressure–temperature–time (*P–T–t*) evolution of the Nagercoil Block and place the findings within the context of the geological evolution of southern India. Further, we suggest that new growth of monazite can occur during both the prograde (melt producing) evolution of migmatites via incongruent melting reactions consuming apatite, as well as during the retrograde path from crystallisation of melt.

2. Geological setting

Palaeogeographic reconstructions of Gondwana have southern India and its close neighbours, Madagascar, Sri Lanka and Antarctica, located at the junction between several orogenic belts that formed as the continental fragments of India, Australia, Azania, Kalahari and Antarctica collided during the latest Neoproterozoic (Ediacaran) or Cambrian (Torsvik et al., 2001; Powell and Pisarevsky, 2002; Meert, 2003; Boger and Miller, 2004; Collins and Pisarevsky, 2005; Trindade et al., 2006; Bogdanova et al., 2008; Pisarevsky et al., 2008; Scotese, 2009). Southern India has been subdivided into a series of discrete crustal units based on lithological associations, crystallisation and model ages, provenance and tectonothermal histories (e.g. Plavsa et al., 2012; Collins et al., 2014). From north to south these are: the Salem Block (or Northern Granulite Terrane; Clark et al., 2009b), the Palghat–Cauvery shear system (PCSS; Collins et al., 2007a; Clark et al., 2009a), the Madurai Block, which has itself been subdivided into discrete terranes (Plavsa et al., 2012, 2014) and, furthest to the south, the Trivandrum and Nagercoil Blocks (Santosh, 1996; Collins et al., 2007b; Santosh et al., 2009; Kröner et al., 2015; Fig. 1). Among these, the Nagercoil Block at the southernmost tip of the Indian peninsula has received comparatively little attention and its role and significance in the evolution of the region are uncertain (Santosh et al., 2003, 2006b; Rajesh et al., 2011).

The Nagercoil Block is dominated by massive orthopyroxene-bearing metagranitoids (hereafter charnockites; Rajesh and Santosh, 2012), and has been interpreted by some as a discrete crustal terrane (Santosh, 1996; Santosh et al., 2003). However,

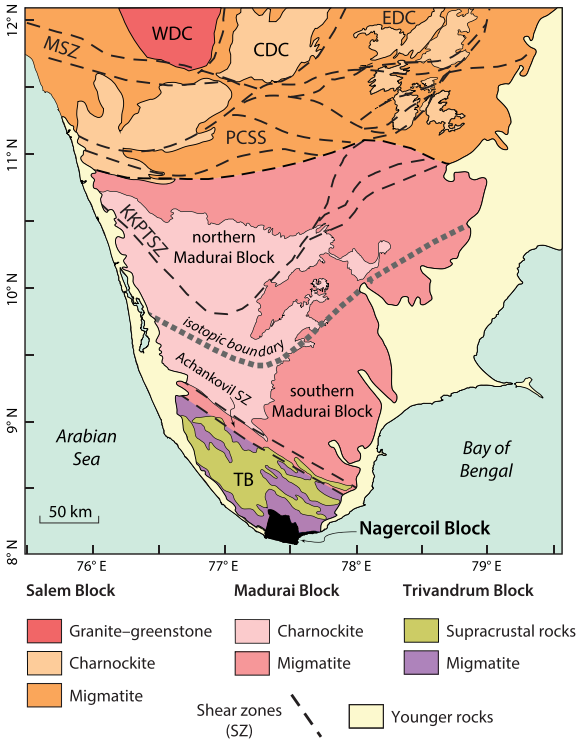

Figure 1. The distribution of terranes and intervening shear zones in Southern India. The Nagercoil Block, which is dominated by charnockite, is at the southernmost tip of the Indian peninsula. WDC – western Dharwar craton; CDC – central Dharwar craton; EDC – eastern Dharwar craton; MSZ – Moyar–Salem–Atur shear zone; PCSS – Palghat–Cauvery shear system; KKPTSZ – Karur Kambam Painavu Trichur shear zone; TB – Trivandrum block. Isotopic boundary between southern and northern Madurai Blocks from Plavsa et al. (2012). Modified after Plavsa et al. (2014).

U–Pb zircon data from the Nagercoil charnockites show they have Palaeoproterozoic protolith ages similar to those reported from 'old' charnockites in the Trivandrum Block (Ghosh et al., 2004; Kröner et al., 2012), consistent with Nd model ages of 2.2–2.6 Ga (Cenki et al., 2004). In addition, age spectra from zircon and monazite within the Nagercoil charnockites are similar to those from metasedimentary gneisses of the Trivandrum Block to the north (Fig. 1), suggesting they may be part of the same tectonic unit (Santosh et al., 2006b).

Using petrologic and geochemical data, including REE, whole rock oxygen isotopes and stable carbon isotopes extracted from CO_2-rich fluid inclusions, Santosh et al. (2009) suggested an igneous origin for the charnockites of the Nagercoil Block. These authors emphasised the adakitic affinities of these rocks and noted their similarities to arc-related charnockites in the Madurai Block, proposing an origin via Pacific-type subduction immediately prior to the amalgamation of Gondwana. In a more recent study Rajesh et al. (2011) interpreted the charnockites to have a metamorphic origin, whose igneous protoliths are suggested to have been granitic plutons derived from partial melting of hydrated basalts (amphibolites) in a subduction zone setting. The high-grade metamorphic event that formed garnet and orthopyroxene is considered to have occurred during the Ediacaran to Cambrian, with garnet growing only in areas where granite had incorporated supracrustal lithologies (Rajesh et al., 2011).

There have been few studies that attempt to constrain the conditions of metamorphism in the Nagercoil Block. Santosh et al. (2003) used conventional thermobarometric methods (garnet–orthopyroxene–plagioclase–quartz barometry and garnet–orthopyroxene thermometry) on the Nagercoil charnockites to propose peak metamorphic conditions of around 4–6 kbar at

temperatures of 700–900 °C (see their Fig. 5). These authors suggested the retrograde *P–T* path was characterised by isothermal decompression from 6 to 4 kbar. However, there are no studies constraining the *P–T* evolution using modern phase equilibria modelling, and there are no detailed datasets constraining provenance or metamorphic history using metasedimentary rocks from the Nagercoil Block.

3. Sample description

The sample selected for detailed study (I12–005a) was collected from a metapelitic raft, around 20 m in length, within a charnockite quarry at Kottaram (77°30′57″E, 8°7′48″N) (Fig. 2a). Garnet is enriched in the charnockite adjacent to, and up to several metres from, the contact with the metapelitic raft. Sample I12–005a contains conspicuous porphyroblasts of garnet and prismatic sillimanite, the latter defining a strong foliation that wraps garnet.

In thin section, sample I12–005a comprises coarser-grained layers (generally 5–15 mm thick) rich in feldspar and garnet that are separated by finer-grained and thinner aluminous layers (up to 2 mm thick) dominated by sillimanite, spinel and cordierite, in which sillimanite defines a prominent foliation (Fig. 2b). Garnet forms porphyroblasts up to 10 mm across that are wrapped by this foliation, and some of the porphyroblasts are flattened slightly. Garnet contains inclusions of quartz and feldspar, sillimanite, ilmenite/magnetite, green spinel, zircon and monazite. Sillimanite inclusions are scarce in the cores of garnet where they show no strong preferred orientation, becoming more abundant at the margins where they are aligned parallel to the matrix foliation (Fig. 2c). Perthite and plagioclase within the coarser-grained garnet-bearing domains are anhedral and generally 0.5–4 mm in diameter. Feldspar grains show weak undulose extinction.

Prismatic sillimanite within the aluminous domains is up to 3 mm long and spatially associated with blocky to cuspate grains of magnetite, composite grains of magnetite and green spinel and rare isolated grains of spinel. In some cases sillimanite is replaced by vermicular intergrowths of spinel and cordierite at its margins. In almost all instances, sillimanite, spinel and magnetite are surrounded by cordierite (Fig. 2c,d). Garnet is variably replaced at its margins by cordierite, particularly where it is near sillimanite and spinel (Fig. 2c,d). Quartz is absent from the matrix and occurs only as inclusions, mainly within garnet. Cordierite only occurs replacing other phases, principally sillimanite, magnetite, spinel and garnet. Biotite forms smaller (<1 mm long) elongate grains that are generally aligned within the foliation, and larger (>1 mm) stubby grains that are at a high angle to the foliation. Both variants appear to have grown across cordierite.

We interpret these petrographic features as evidence for partial melting and melt loss with limited retrograde reaction. The coarser-grained layers are interpreted as deformed K-feldspar-rich leucosomes containing peritectic garnet that grew in equilibrium with sillimanite, spinel and magnetite. The aluminous layers represent the residual portion of the rock. The peak assemblage is interpreted as garnet–K-feldspar–sillimanite–magnetite–plagioclase–ilmenite–spinel–melt. The growth of cordierite replacing sillimanite, spinel–magnetite and garnet, and rare

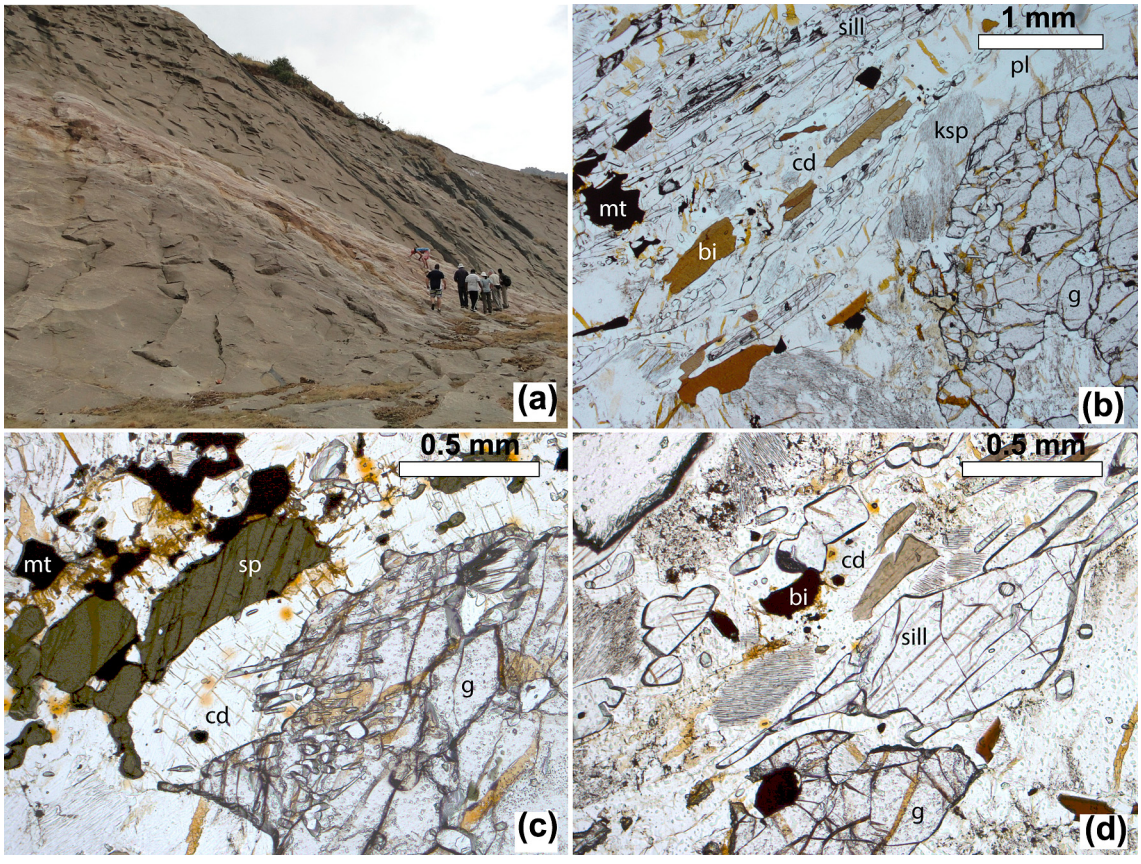

Figure 2. Field and petrographic features of sample I12–005a. (a) Charnockite quarry at Kottaram with geologists standing on the elongate metapelite raft from which sample I12–005a was collected. (b) Porphyroblast of garnet associated with coarse-grained feldspar (leucosome; bottom and right) and an aluminous layer rich in prismatic sillimanite with magnetite (residuum; left and top). Sillimanite, which defines a foliation that wraps the garnet porphyroblast, is partially replaced by cordierite. (c) Replacement of garnet and spinel by cordierite. The garnet rim contains numerous inclusion of sillimanite with a strong preferred orientation. (d) Sillimanite and garnet (bottom centre) replaced by cordierite. Grains of perthitic feldspar are also present, along with late biotite.

symplectites of spinel–cordierite replacing sillimanite, are suggested to record high-temperature retrograde reaction in the presence of melt. Late biotite probably records crystallisation of the last vestiges of melt.

4. Phase equilibria modelling

Phase equilibria calculations are based on the major element oxide bulk composition of sample I12–005a as determined by XRF analysis, in which the concentrations of ferric and ferrous iron were determined by titration (Table 1). Calculations using THERMOCALC (Powell and Holland, 1988) are in the Na_2O–CaO–K_2O–FeO–MgO–Al_2O_3–SiO_2–H_2O–TiO_2–O (NCKFMASHTO) model system and use the end-member thermodynamic data of Holland and Powell (2011) (ds62 dataset as generated on 06/02/14) and *a–X* models detailed in White et al. (2014a). Although Mn has now been incorporated into these solution models (White et al., 2014b), it has minimal effect at high temperatures and so was not considered.

A *P–T* pseudosection using the loss on ignition (LOI) as determined by XRF as a direct proxy for the H_2O content contains fields appropriate to the inferred peak assemblage (with or without magnetite) at conditions of around 6.5–9 kbar and 850–950 °C (Fig. 3a). However, an H_2O-saturated ('wet') solidus is predicted to occur between 650 and 700 °C that is inconsistent with the residual nature of the rock and the preservation of high-*T* anhydrous minerals (White and Powell, 2002). This may be due to post-peak hydration of the sample (as evidenced by minor pinite in cordierite and sericite in feldspar), inclusion of additional volatile species (principally CO_2 in cordierite, F in biotite), errors in the analysed LOI and/or issues with the solution model for melt (e.g. Kelsey and Hand, 2015). Consequently, *T–X* (Fig. 3b) and *P–X* (Fig. 3c) pseudosections varying the H_2O content were calculated in order to constrain the amount of H_2O present, such that the calculated solidus intersects appropriate fields containing those minerals preserved within sample I12–005a. In both cases, the phase equilibria are consistent with H_2O contents 30% or less of the measured LOI (Fig. 3b,c).

Fig. 3d shows a *P–T* pseudosection for a (residual) composition with H_2O content [$M(H_2O)$] 0.25 times the measured LOI. This diagram is characterised by an elevated H_2O-absent solidus that occurs at temperatures between 775 and 850 °C and by four NCKFMASHTO divariant fields (labelled with emboldened phase abbreviations on Fig. 3) that correspond to, from relatively low-to high-*T*, the KFMASH univariant reactions:

$$bi + sill + q = g + cd + ksp + liq \quad (1)$$

$$bi + sill + g = cd + sp + ksp + liq \quad (2)$$

$$sill + g + ksp = cd + sp + liq \quad (3)$$

$$g + cd + ksp = opx + sp + q + liq \quad (4)$$

A field for the inferred peak assemblage occurs at pressures of around 6–8 kbar and temperatures in excess of 900 °C. At pressures below this field cordierite is predicted to be stable and, at lower temperatures, spinel does not occur (although spinel may be stabilized in rocks to lower *T* by the presence of Zn, which cannot currently be modelled). A field containing the peak assemblage plus cordierite intersects the solidus at around 5 kbar and 800–830 °C; at slightly lower *T* biotite is predicted. An example *P–T* path consistent with the petrographic observations is shown in Fig. 3d.

Table 1
Bulk compositions (as mol.%) used in the calculation of the pseudosections shown in Fig. 3.

Figure	H_2O	SiO_2	Al_2O_3	CaO	MgO	FeO	K_2O	Na_2O	TiO_2	O
3a	6.73	53.99	15.91	0.93	5.47	9.90	2.61	2.53	0.75	1.18
3b and 3c (lhs)	6.73	53.99	15.91	0.93	5.47	9.90	2.61	2.53	0.75	1.18
3b and 3c (rhs)	0.01	57.88	17.05	1.00	5.86	10.62	2.80	2.71	0.81	1.27
3d	1.69	56.90	16.77	0.98	5.76	10.44	2.75	2.67	0.79	1.25

5. Geochronology, trace element and O-isotope geochemistry

Zircon, monazite and garnet from sample I12–005a were analysed in order to derive temporal constraints linking the evolution of the main silicate mineral assemblage with partial melting and accessory phase growth. Measurements of zircon and monazite were made on grain separates mounted in epoxy, whereas garnet was measured in thin section. U–Pb isotopic analysis of zircon and monazite used the Sensitive High Resolution Ion Microprobe (SHRIMP) housed at Curtin University (Tables 2 and 3). Trace elements in zircon, monazite and garnet were measured at the LA–ICP–MS facility at the same institution (Table 4). Oxygen isotopes were measured on the Cameca IMS 1280 ion microprobe at the University of Western Australia. Full details of the analytical methods are given in the Supplementary data.

5.1. Morphology of zircon and monazite

Zircon grains from sample I12–005a are rounded to elongate and typically 50–200 μm in the longest dimension. Cathodoluminescence (CL) images identify a variety of textures (Fig. 4a–i) with a range of CL responses. Some grains are characterized by oscillatory-zoned cores with variable CL response typical of zircon grown in a magmatic environment (Hoskin and Black, 2000; Corfu et al., 2003) (Fig. 4a–c). Some grains that are generally mid to light grey in CL show evidence for recrystallization and formation of sector zoning (Fig. 4d–f). Other grains show irregular zoning or broad featureless zones with low CL response that, in some cases, mantle oscillatory-zoned igneous cores (Fig. 4b,c) or light grey CL sector zoned grains (Fig. 4g–i).

Monazite grains from sample I12–005a are typically subequant or irregular in shape and 200–400 μm across (Fig. 5). Backscattered electron (BSE) images show that several grains are zoned. Many show irregular lower BSE response central portions surrounded by brighter BSE regions (e.g. Fig. 5a–c). Others exhibit complex textures with multiple zones of variable BSE response (Fig. 5d,e) or little variation in BSE response (Fig. 5f).

5.2. U–Pb geochronology

Twenty-three analyses of zircon were undertaken; 17 were from rims interpreted to have grown during metamorphism and six were from oscillatory-zoned cores interpreted to be of magmatic origin. Zircon ages from oscillatory-zoned cores are highly discordant (Fig. 6a), typical of partial Pb loss during high-grade metamorphism (Mezger and Krogstad, 1997). The most concordant analysis of an oscillatory-zoned core (analysis 16.1) gives a $^{207}Pb/^{206}Pb$ spot age of 2064 ± 42 Ma. The remaining core analyses define a poorly constrained discordant array from this age towards the younger concordant rim data (Fig. 6a). Most oscillatory-zoned zircon cores have U concentrations in the range 500–1000 ppm (Table 2) with Th/U ratios of 0.02–0.36.

The data from zircon interpreted to be metamorphic, as identified by mid-grey CL sector zoning and low CL featureless zones, show <4% discordance ($^{206}Pb/^{238}U$ vs. $^{207}Pb/^{235}U$, Table 2) and give $^{206}Pb/^{238}U$ ages that are spread along concordia between around 600 to 510 Ma (Fig. 6b). Metamorphic zircons possess from around

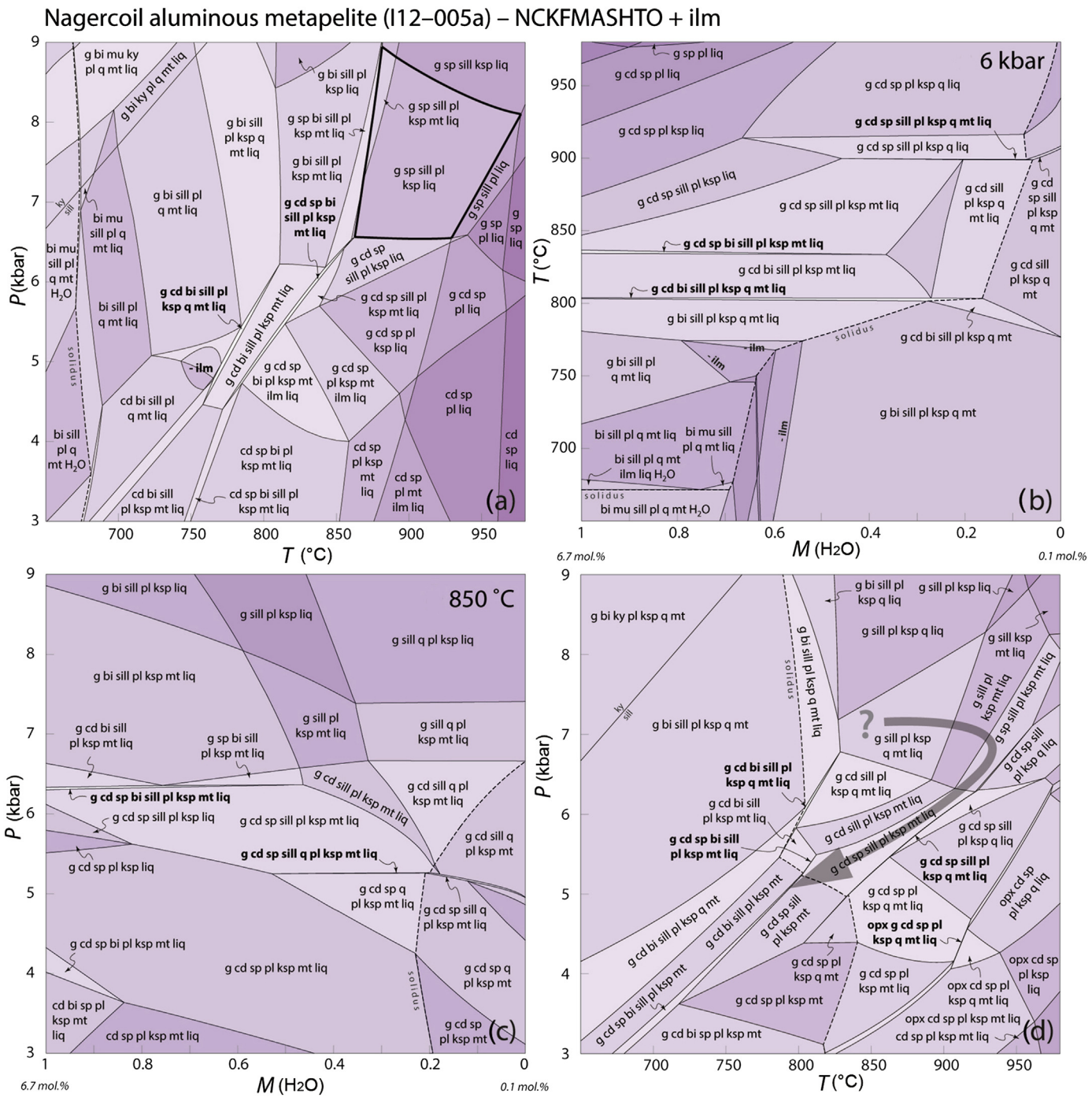

Figure 3. Phase equilibria modelling results based on the composition of the aluminous metapelite sample I12–005. (a) *P*–*T* pseudosection assuming an H_2O content equivalent to the loss on ignition (LOI) as measured by XRF. The inferred peak field, with or without magnetite, is outlined in bold, although this composition predicts an H_2O-saturated solidus suggesting the H_2O content is unrealistically high for peak conditions. (b) Isobaric ($P = 6$ kbar) *T*–*X* pseudosection with variable H_2O content ranging from that used in the calculation of (a) [$M(H_2O) = 1$] to much lower values of 0.1 mol.%; [$M(H_2O) = 0$]. Cordierite is not predicted to be stable at the solidus for $M(H_2O)$ less than around 0.3. (c) Isothermal ($T = 850$ °C) *P*–*X* pseudosection with variable H_2O content as described for (b). At 850 °C a solidus is present only for $M(H_2O)$ of around 0.25 or less. (d). *P*–*T* pseudosection assuming an H_2O content one quarter of the value based on measured LOI, a reasonable estimate based on the *T*–*X* and *P*–*X* diagrams shown in (b) and (c). An example *P*–*T* path is shown that is consistent with petrographic constraints, although the prograde segment is largely unconstrained. The bulk compositions used in the calculations of each phase diagram are given in Table 1.

600 to 2900 ppm U and have Th/U ratios of 0.01–0.16 (Fig. 6b). The two main textures identified in the CL images show a correlation with both U–Pb age and Th/U ratio. Mid-grey CL sector zoned zircon (Fig. 4d–f) typically give the oldest ages, ranging from 639 ± 10 to 547 ± 10 Ma ($n = 9$). The majority of these grains (7 out of 9) have low U concentrations (<800 ppm) and Th/U between 0.01 and 0.02 (Table 2). Metamorphic zircon that is dark in CL and generally shows broad, featureless zoning (Fig. 4c, g–i) typically give the youngest ages, ranging from 580 ± 6 to 531 ± 5 Ma ($n = 8$). These grains have the highest U concentrations (1701–2882 ppm) and Th/U between 0.06 and 0.15 (Table 2). Fig. 6b shows that the U–Pb data for metamorphic zircon are correlated with Th/U ratio. Although there are probably insufficient data on the probability density distribution of the metamorphic zircon ages, the most

Table 2
SHRIMP zircon U–Pb data.

Spot	$^{204}Pb/^{206}Pb$	±%	$^{206}Pb_c$ (%)	U (ppm)	Th (ppm)	204 corr. $^{206}Pb^*$ (ppm)	$^{232}Th/^{238}U$	±%	$^{206}Pb/^{238}U$ age$^{(1)}$	$^{207}Pb/^{235}U$ age$^{(1)}$	$^{207}Pb/^{206}Pb$ age$^{(1)}$	U–Pb % Disc.	Pb–Pb % Disc.	$^{238}U/^{206}Pb^*$$^{(1)}$	±%	$^{207}Pb^*/^{206}Pb^*$$^{(1)}$	±%	$^{207}Pb^*/^{235}U$$^{(1)}$	±%	$^{206}Pb^*/^{238}U$$^{(1)}$	±%	Corr.
125A-16.2	2.9E-5	33	0.05	2002	109	148	0.06	0.53	531	529	517	0	−3	11.6	1.0	0.058	0.8	0.68	1.3	0.086	1.0	0.8
125A-12.2	2.5E-5	33	0.04	2093	263	158	0.13	0.15	544	537	509	−1	−7	11.4	1.2	0.057	0.8	0.70	1.4	0.088	1.2	0.8
125A-7.1	2.8E-5	33	0.05	2040	222	155	0.11	0.16	545	546	551	0	+1	11.3	1.0	0.059	0.5	0.71	1.1	0.088	1.0	0.9
125A-4.1	1.1E-5	45	0.02	2808	200	213	0.07	0.17	546	547	549	0	+1	11.3	1.3	0.059	0.9	0.71	1.6	0.088	1.3	0.8
125A-9.1	8.6E-5	35	0.15	538	6	41	0.01	1.97	547	531	461	−3	−19	11.3	2.0	0.056	3.1	0.69	3.7	0.089	2.0	0.5
125A-14.1	1.8E-5	35	0.03	2882	244	221	0.09	0.16	551	540	497	−2	−11	11.2	1.7	0.057	0.4	0.70	1.7	0.089	1.7	1.0
125A-13.1	2.8E-5	33	0.05	1940	155	149	0.08	0.19	552	551	551	0	−0	11.2	1.7	0.059	1.3	0.72	2.2	0.089	1.7	0.8
125A-12.1	1.1E-5	50	0.02	1944	208	150	0.11	0.17	553	554	557	0	+1	11.2	1.0	0.059	0.8	0.73	1.3	0.090	1.0	0.8
125A-7.2	2.9E-5	45	0.05	1138	174	88	0.16	0.19	553	552	547	0	−1	11.2	1.6	0.058	2.1	0.72	2.6	0.090	1.6	0.6
125A-8.1	1.4E-5	45	0.02	2265	132	176	0.06	0.21	559	551	517	−1	−8	11.0	1.7	0.058	0.5	0.72	1.7	0.091	1.7	1.0
125A-5.1	−3.4E-6	100	–	1701	239	137	0.15	0.27	580	577	567	0	−2	10.6	1.0	0.059	1.2	0.77	1.6	0.094	1.0	0.7
125A-11.1	7.0E-5	38	0.12	613	4	50	0.01	1.23	586	596	638	+9	+9	10.5	1.7	0.061	1.9	0.80	2.6	0.095	1.7	0.7
125A-1.1	4.8E-5	41	0.09	761	5	62	0.01	1.02	586	583	573	0	−2	10.5	1.1	0.059	1.3	0.78	1.7	0.095	1.1	0.6
125A-3.1	3.7E-5	45	0.07	739	14	61	0.02	0.60	596	608	652	2	+9	10.3	3.0	0.061	4.3	0.82	5.2	0.097	3.0	0.6
125A-6.1	8.2E-6	100	0.01	705	4	59	0.01	1.10	598	606	636	1	+6	10.3	2.5	0.061	1.9	0.82	3.1	0.097	2.5	0.8
125A-10.1	2.3E-5	58	0.04	739	9	66	0.01	0.80	635	624	581	−2	−10	9.7	2.4	0.059	4.9	0.85	5.5	0.104	2.4	0.4
125A-2.1	9.9E-5	29	0.18	627	5	56	0.01	1.74	639	613	519	−4	−24	9.6	1.7	0.058	2.8	0.83	3.3	0.104	1.7	0.5
125A-15.1	8.6E-5	38	0.15	479	30	44	0.06	0.50	650	794	1222	+49	+49	9.4	2.1	0.081	2.8	1.19	3.5	0.106	2.1	0.6
125A-21.1	3.0E-5	50	0.05	657	15	81	0.02	0.68	860	1093	1592	+49	+48	7.0	5.4	0.098	6.9	1.93	8.7	0.143	5.4	0.6
125A-19.1	1.0E-4	30	0.19	399	79	58	0.21	0.60	1000	1284	1797	+46	+48	6.0	13.3	0.110	10.6	2.54	17.0	0.168	13.3	0.8
125A-17.1	8.7E-5	25	0.15	570	46	85	0.08	0.77	1033	1315	1809	+46	+46	5.8	8.3	0.111	7.4	2.65	11.1	0.174	8.3	0.7
125A-18.1	4.1E-5	21	0.07	1732	444	281	0.26	0.25	1114	1306	1638	+35	+35	5.3	1.7	0.101	1.9	2.62	2.5	0.189	1.7	0.7
125A-16.1	-6.3E-6	50	–	985	345	293	0.36	1.48	1915	1988	2064	+8	+8	2.9	2.5	0.127	2.4	6.08	3.5	0.346	2.5	0.7

Errors are 1σ; Pb_c and Pb^* indicate the common and radiogenic portions, respectively. Disc. = discordance, Corr. = correlation.
Error in standard calibration was 0.29% (not included in above errors but required when comparing data from different mounts).
(1) Common Pb corrected using measured ^{204}Pb.

concordant data from low CL-response overgrowth show a peak at around 545 Ma (Fig. 6c).

Twenty-nine monazite grains were analysed covering a range of textures identified using BSE imaging. The $^{206}Pb/^{238}U$ data from monazite are spread along concordia from 584 to 506 Ma, with all analyses within 2% of concordance ($^{206}Pb/^{238}U$ vs. $^{207}Pb/^{235}U$, Table 3). While the monazite data form an almost continuous spread, two chemically different groups can be identified corresponding to relative probability age peaks at c. 570 and c. 535 Ma (Fig. 6d). There is a morphological (and compositional) correlation within this spread, with older monazite U–Pb ages typically from the dark BSE portions of the grains, corresponding to low Th/U ratios, and younger ages corresponding to higher BSE response and Th/U ratios. Monazite grains with $^{206}Pb/^{238}U$ spot ages from 584 to 563 Ma have Th/U ratios ranging from 5 to 10, whereas younger monazite with $^{206}Pb/^{238}U$ spot ages from 559 to 506 Ma have Th/U ratios ranging from 8 to 19 (Table 3).

5.3. Trace element geochemistry

Due to the complex nature of the zircon grains in this study, including evidence for recrystallisation and multiple zonation, all but 12 laser ablation analyses resulted in mixed analyses (as identified by interrogating time-resolved data). However, these 12 analyses cover the major zircon types identified both using textural criteria and U–Pb isotopic composition.

Three analyses of oscillatory-zoned zircon cores are relatively enriched in Yb ($Yb_N = 215–567$) and are characterised by steep positive HREE profiles ($Yb_N/Dy_N = 2.9–5.0$) and Eu/Eu* [$=Eu_N/(Gd_N–Sm_N) \times 0.5$] of 0.4–0.12 (Fig. 7a). The chondrite-normalised REE composition of metamorphic zircon indicates two different groups, which correspond to subdivisions previously identified using textural and compositional criteria. The first group, with zircon $^{206}Pb/^{238}U$ spot ages from 639 to 586 Ma, contain relatively high concentrations of middle to heavy REE ($Yb_N = 36–143$) and show a distinct 'hump' in the MREE (Dy_N ranging from 150 to 340), resulting in a slightly negative middle to heavy REE slope with Yb_N/Dy_N of 0.2–0.5 (Fig. 7a). The second group, with zircon $^{206}Pb/^{238}U$ spot ages from 559 to 531 Ma, also shows a negative middle to heavy REE slope (Yb_N/Dy_N of 0.3–0.6) but contains middle to heavy REE concentrations that are around an order of magnitude lower (Fig. 7a). The two groups also show a clear difference in the magnitude of the negative Eu anomaly; the older metamorphic zircon has Eu/Eu* values of 0.09–0.11, and the younger metamorphic zircon has values of 0.002–0.02.

To further evaluate the importance of the REE data in metamorphic zircon, three garnets from the sample were also analysed *in situ*; for each grain two cores and two rims were analysed. The three garnet grains exhibit some inter- and intra-grain compositional variation with relatively high, intermediate and low chondrite-normalised HREE concentrations (Fig. 7b). Garnet 1 shows the highest HREE values ($Yb_N = 108–153$) and has a slightly positive middle to heavy REE slope with Yb_N/Dy_N of 1.2–1.5. Garnet 2 contains the lowest HREE contents ($Yb_N = 21.5–32.3$) and has a slightly negative middle to heavy REE slope ($Yb_N/Dy_N = 0.3–0.5$). Neither grain shows any statistically meaningful variation between core and rim compositions. Garnet 3 shows some core to rim variation, with the core of the grain corresponding to the composition of garnet 1 (Yb_N of 124–129 and Yb_N/Dy_N of 1.5–1.6) (Fig. 7b). The rim of garnet 3 is depleted compared to the core ($Yb_N = 46–64$; $Yb_N/Dy_N = 0.5–0.7$). All garnet grains exhibit a similar negative Eu anomaly with Eu/Eu* between 0.006 and 0.014.

Monazite grains have variable trace element compositions that are related to the two different age populations. All grains have typical steep negative chondrite-normalised REE slopes and a pronounced but variable negative Eu anomaly (Fig. 7c). Whilst some correlation between the Th/U ratio and U–Pb age data was identified,

Table 3
SHRIMP monazite U–Pb data.

Spot	^{206}Pb (cts/sec)	^{232}Th/^{238}U	±%	^{206}Pb/^{238}U age$^{(1)}$		^{207}Pb/^{206}Pb age$^{(1)}$		^{207}Pb/^{235}U age$^{(1)}$		% Disc.	Total ^{238}U/^{206}Pb	±%	Total ^{207}Pb/^{206}Pb	±%	^{207}Pb*/^{235}U	±%	^{206}Pb*/^{238}U	±%	Corr.
05A-3.2	4569	9	3.0	506	±9	515	±15	507	±10	+0	12.25	1.9	0.0576	0.50	0.65	2.0	0.0816	1.9	0.9
05A-2.2	4728	11	3.0	525	±10	518	±22	523	±11	−0	11.79	1.9	0.0577	0.55	0.67	2.2	0.0848	1.9	0.9
05A-14.1	4650	16	3.0	529	±10	520	±16	527	±11	−0	11.70	1.9	0.0577	0.50	0.68	2.0	0.0855	1.9	0.9
05A-14.2	5269	16	3.0	531	±10	499	±15	525	±11	−1	11.65	1.9	0.0572	0.47	0.68	2.0	0.0858	1.9	0.9
05A-7.2	5132	17	3.0	532	±10	527	±27	531	±12	−0	11.63	1.9	0.0579	1.19	0.69	2.3	0.0860	1.9	0.8
05A-20.2	4869	13	3.0	533	±10	516	±14	530	±11	−1	11.60	1.9	0.0576	0.49	0.69	2.0	0.0862	1.9	0.9
05A-18.2	4024	8	3.0	535	±10	561	±14	540	±11	+1	11.55	1.9	0.0588	0.53	0.70	2.0	0.0866	1.9	0.9
05A-16.2	3892	10	3.0	536	±10	538	±15	536	±11	+0	11.54	1.9	0.0582	0.54	0.70	2.0	0.0866	1.9	0.9
05A-13.2	5168	19	3.1	537	±10	543	±22	538	±12	+0	11.51	2.0	0.0584	0.47	0.70	2.3	0.0869	2.0	0.9
05A-10.2	4523	12	3.0	540	±10	552	±12	542	±11	+0	11.44	1.9	0.0586	0.50	0.71	2.0	0.0874	1.9	1.0
05A-15.2	4302	18	3.0	541	±10	544	±16	542	±11	+0	11.42	2.0	0.0584	0.51	0.70	2.1	0.0876	2.0	0.9
05A-10.1	4539	9	3.0	543	±10	548	±14	544	±11	+0	11.39	1.9	0.0585	0.56	0.71	2.0	0.0878	1.9	0.9
05A-8.2	4068	14	3.0	549	±10	558	±14	551	±11	+0	11.24	1.9	0.0587	0.53	0.72	2.0	0.0890	1.9	0.9
05A-17.2	4553	12	3.0	552	±10	562	±13	554	±11	+0	11.19	1.9	0.0589	0.50	0.73	2.0	0.0894	1.9	1.0
05A-3.1	4582	9	3.0	558	±10	607	±12	568	±11	+2	11.05	1.9	0.0601	0.49	0.75	2.0	0.0905	1.9	1.0
05A-15.1	3359	12	3.0	559	±10	569	±17	561	±12	+0	11.04	1.9	0.0590	0.58	0.74	2.1	0.0906	1.9	0.9
05A-19.2	4458	8	3.0	563	±10	629	±13	576	±12	+2	10.96	1.9	0.0607	0.50	0.76	2.0	0.0913	1.9	1.0
05A-19.1	4864	6	3.0	564	±10	583	±11	568	±11	+1	10.93	1.9	0.0594	0.48	0.75	2.0	0.0915	1.9	1.0
05A-5.1	3928	8	3.0	566	±10	571	±12	567	±11	+0	10.89	1.9	0.0591	0.53	0.75	2.0	0.0918	1.9	1.0
05A-20.1	4145	8	3.0	567	±10	564	±11	566	±11	−0	10.88	1.9	0.0589	0.52	0.75	2.0	0.0919	1.9	1.0
05A-9.1	4573	5	3.0	567	±10	589	±11	571	±11	+1	10.88	1.9	0.0596	0.49	0.76	2.0	0.0919	1.9	1.0
05A-6.2	4506	7	3.0	569	±10	534	±12	562	±11	−1	10.83	1.9	0.0581	0.50	0.74	2.0	0.0923	1.9	1.0
05A-12.1	4127	8	3.0	572	±11	581	±21	574	±12	+0	10.78	1.9	0.0594	0.95	0.76	2.2	0.0928	1.9	0.9
05A-8.1	4642	7	3.0	574	±11	566	±12	572	±11	−0	10.75	1.9	0.0590	0.49	0.76	2.0	0.0931	1.9	1.0
05A-5.2	4691	6	3.0	574	±11	571	±11	573	±11	−0	10.74	1.9	0.0591	0.49	0.76	2.0	0.0931	1.9	1.0
05A-1.2	4434	8	3.0	576	±11	579	±13	576	±12	+0	10.71	1.9	0.0593	0.50	0.76	2.0	0.0934	1.9	1.0
05A-18.1	5340	6	3.0	576	±11	558	±11	572	±11	−1	10.70	1.9	0.0588	0.46	0.76	2.0	0.0934	1.9	1.0
05A-1.1	4134	10	3.0	578	±11	582	±13	579	±12	+0	10.65	1.9	0.0594	0.52	0.77	2.0	0.0939	1.9	1.0
05A-9.2	6162	5	3.0	580	±11	602	±9	584	±11	+1	10.62	1.9	0.0599	0.42	0.78	2.0	0.0942	1.9	1.0
05A-6.1	5420	7	3.0	581	±11	592	±19	584	±12	+0	10.60	1.9	0.0597	0.88	0.78	2.1	0.0944	1.9	0.9
05A-2.1	5200	6	3.0	584	±11	576	±10	583	±12	−0	10.54	1.9	0.0592	0.46	0.78	2.0	0.0949	1.9	1.0

Errors are 1σ; Pb_c and Pb^* indicate the common and radiogenic portions, respectively. Disc. = discordance, Corr. = correlation.
Error in standard calibration was 0.43% (not included in above errors but required when comparing data from different mounts).
(1) Common Pb corrected using measured ^{204}Pb.

Table 4
REE concentrations of selected grains of zircon, monazite and garnet normalised to CI chondrite values of McDonough and Sun (1995). Ages for zircon and monazite are $^{206}Pb/^{238}U$.

	Age (Ma)	La	Ce	Pr	Nd	Sm	Eu	Gd	Tb	Dy	Ho	Er	Tm	Yb	Lu
Zircon															
5A-16.2	531	0.0	2.2	1.0	4.1	30.7	0.1	35	32	26	25	20	19	17	16
5A-12.2	545	0.0	1.6	0.6	2.7	18.4	0.0	27	24	19	11	11	10	11	8
5A-7.1	546	0.1	2.9	1.1	3.6	28.7	0.6	39	36	25	16	21	15	14	14
5A-4.1	559	0.0	1.6	0.9	4.2	30.7	0.4	40	37	31	18	12	10	8	5
5A-5.1	586	bd	0.5	0.2	1.1	20.2	8.3	127	260	300	196	137	90	83	103
5A-11.1	586	0.0	0.4	0.2	0.4	8.6	3.4	62	129	150	85	55	51	36	46
5A-1.1	596	bd	0.7	0.5	1.5	22.2	9.1	147	276	313	230	196	165	143	139
5A-3.1	598	bd	0.7	0.4	1.6	26.3	11.0	170	339	340	194	140	109	86	105
5A-10.1	639	bd	0.5	0.1	0.5	7.7	3.6	70	156	197	140	102	90	70	64
5A-15.1	860	bd	0.9	0.4	2.1	16.9	1.1	45	60	75	63	89	128	215	296
5A-21.1	1000	0.1	2.7	0.2	0.8	9.6	3.8	52	113	159	153	218	322	498	704
5A-19.1	1033	0.0	0.8	0.0	0.7	7.5	2.0	40	71	113	148	216	384	567	794
Monazite															
05A-13.2	537	403,068	382,202	374,635	330,681	133,855	423	38,708	8760	1850	394	108	73	18	29
05A-10.2	542	418,833	382,172	362,290	305,924	134,058	547	47,304	10,193	2283	504	130	87	25	36
05A-15.2	545	440,136	382,172	346,801	275,199	126,920	2171	48,576	10,829	2575	629	163	103	25	38
05A-10.1	547	541,116	382,195	310,325	254,863	133,583	594	61,089	18,799	4808	1038	251	114	39	59
05A-8.2	548	470,814	382,172	326,150	258,621	117,403	2289	51,221	12,523	2802	640	165	99	30	42
05A-17.2	549	406,476	382,182	371,605	357,206	129,708	485	22,721	5433	1144	297	102	78	15	20
05A-3.1	552	452,066	382,180	345,791	301,724	113,936	839	25,025	5950	1141	273	86	67	15	23
05A-15.1	553	416,702	382,178	371,942	330,460	111,149	1014	24,654	6691	1533	401	128	73	19	21
05A-19.2	559	458,458	382,172	333,446	249,779	112,848	957	43,947	8603	1821	461	143	91	26	35
05A-19.1	565	491,692	382,172	337,262	248,453	118,015	5613	57,782	14,788	3795	869	210	102	35	46
05A-5.1	565	453,771	382,188	341,302	291,114	136,846	859	49,237	11,680	2625	570	151	86	22	40
05A-20.1	565	525,778	382,190	316,947	251,105	124,541	11,054	59,766	20,496	5665	1336	347	152	60	60
05A-9.1	573	510,439	382,172	327,497	234,306	118,491	6768	61,750	16,309	3885	853	192	100	34	46
05A-6.2	575	470,388	382,187	336,588	279,399	133,923	3304	56,205	16,116	4108	942	230	102	35	49
05A-12.1	576	537,282	382,192	302,694	247,790	118,967	7304	55,341	18,353	5637	1514	459	174	67	59
05A-8.1	577	576,055	382,172	285,859	226,569	120,870	10,175	69,786	24,545	5941	1427	374	154	65	73
05A-5.2	578	546,229	382,200	294,725	222,812	122,502	10,173	69,023	28,375	7042	1642	384	140	59	71
05A-1.2	579	562,846	382,172	287,093	211,096	112,305	10,564	73,347	27,273	6625	1552	378	157	60	71
05A-18.1	579	527,056	382,172	308,081	223,475	111,217	5429	51,628	12,204	2621	538	129	81	26	35
05A-1.1	580	557,733	382,183	305,275	245,137	122,978	8695	62,970	19,890	4998	1094	258	108	41	56
05A-9.2	583	557,307	382,193	293,715	221,927	120,462	10,679	68,566	27,355	6786	1579	388	151	66	70
05A-6.1	585	571,368	382,198	292,480	221,485	127,940	12,679	70,651	32,259	7857	1876	437	157	63	77
Garnet															
5a_grt1_rim	–	0.0	0.0	1.0	5.3	73.8	0.8	101	88	98	96	128	149	153	154
5a_grt1_rim	–	0.0	0.0	0.8	3.6	59.0	0.8	97	91	92	85	108	94	108	104
5a_grt1_core	–	0.0	0.0	0.1	2.0	69.3	0.7	101	86	90	96	121	146	130	116
5a_grt1_core	–	0.0	0.0	0.1	1.9	59.0	0.9	92	79	85	91	118	112	132	108
5a_grt2_rim	–	0.0	0.0	1.1	7.0	78.2	0.9	111	93	85	66	48	40	29	26
5a_grt2_rim	–	0.1	0.0	2.0	8.6	91.4	1.4	110	89	79	58	42	38	26	24
5a_grt2_core	–	0.0	0.0	0.5	4.0	70.5	0.8	94	82	69	50	44	39	22	33
5a_grt2_core	–	0.0	0.1	1.2	4.6	74.7	1.0	93	80	65	46	45	33	32	26
5a_grt3_rim	–	0.0	0.3	1.1	6.3	77.1	0.8	114	98	93	79	60	67	46	43
5a_grt3_rim	–	0.0	0.0	0.4	2.9	55.0	0.9	97	88	90	73	66	56	65	59
5a_grt3_core	–	0.0	0.0	0.1	2.2	67.5	0.7	84	74	80	92	115	120	124	118
5a_grt3_core	–	0.0	0.0	0.1	2.3	68.5	0.4	80	73	87	104	119	113	129	123

the clearest chemical criteria for the different monazite age groups are the REE, particularly the Yb concentration and Eu/Eu* ratio (Figs. 6e,f and 7c,d). Yb_N and Eu anomaly are correlated (Fig. 7d) highlighting two distinct chemical groups, separated by a group of more widely spread analyses, that may represent either partially recrystallized monazite or mixed laser ablation analyses (Fig. 7d). These two clearly defined groups correspond to the two relative probability age groups identified in the SHRIMP U–Pb data. The first group ($Yb_N = 55–75$; $Eu/Eu^* = 0.10–0.13$) gave $^{206}Pb/^{238}U$ spot ages from 584 to 564 Ma with a weighted mean $^{206}Pb/^{238}U$ age of 572 ± 5 Ma (MSWD = 2.5, $n = 12$). The second group ($Yb_N = 14–39$; $Eu/Eu^* = 0.005–0.03$) yielded $^{206}Pb/^{238}U$ spot ages from 569 to 506 Ma, with seven out of nine of the analyses forming a distinct age group with a weighted mean $^{206}Pb/^{238}U$ age of 536 ± 4 Ma (MSWD = 0.83, $n = 7$). In addition to these differences, there is also a small variation in the concentration of Ca between the two groups of monazite, with the older group containing 6700–4260 ppm (mean = 5345 ppm), and the younger group 5990–3660 ppm (mean = 4224 ppm).

5.4. Oxygen isotope composition

Oxygen isotope analyses from zircon in the metapelite show $\delta^{18}O$ values of around 9.0–9.6‰. These are around 2‰ higher than those in the enclosing charnockite ($\delta^{18}O$ = 6.8–7.8‰; Clark et al., unpublished data). These data are consistent with the whole rock O-isotope data collected previously from this locality (Rajesh et al., 2011).

6. Discussion

6.1. P–T constraints

Phase equilibrium modelling of sample I12–005a suggests that the interpreted peak metamorphic assemblage records pressures of around 6–8 kbar and temperatures of 900–950 °C. These results are consistent with extreme metamorphism at ultrahigh temperature (Harley, 1998; Kelsey, 2008; Clark et al., 2011; Kelsey and Hand, 2015). Although the rock is residual and the modelled composition

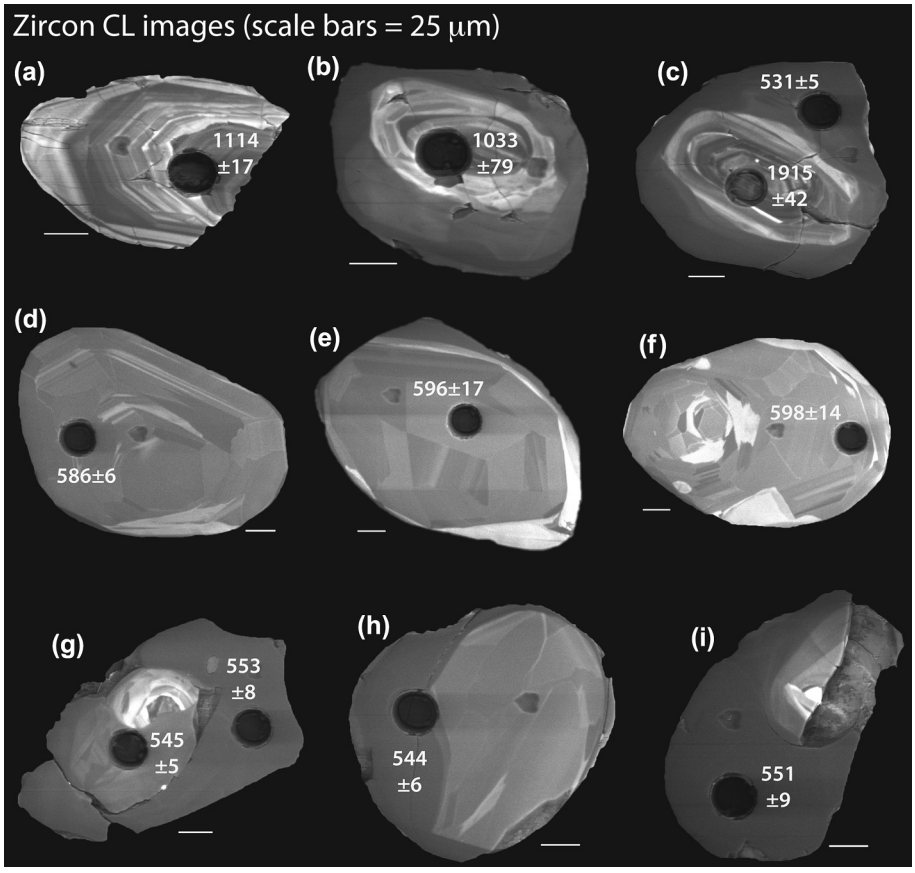

Figure 4. Cathodoluminesence images illustrating the range of zircon morphologies. The SHRIMP $^{206}Pb/^{238}U$ ages and 1σ errors are given. Full analytical results are given in Table 2.

is not strictly valid for constraining conditions prior to the metamorphic peak, the lack of evidence for the prograde presence of kyanite or cordierite (e.g. as inclusions) suggests the high temperature (suprasolidus) segment of the prograde *P*–*T* path did not pass through pressures much higher or lower than those at the metamorphic peak (Fig. 3d). The late growth of cordierite, including cordierite–spinel intergrowths replacing sillimanite, then biotite is consistent with retrograde decompression at high temperature and the crossing of an elevated solidus at conditions of around 5 kbar and 800 °C. The peak conditions and the example clockwise *P*–*T*

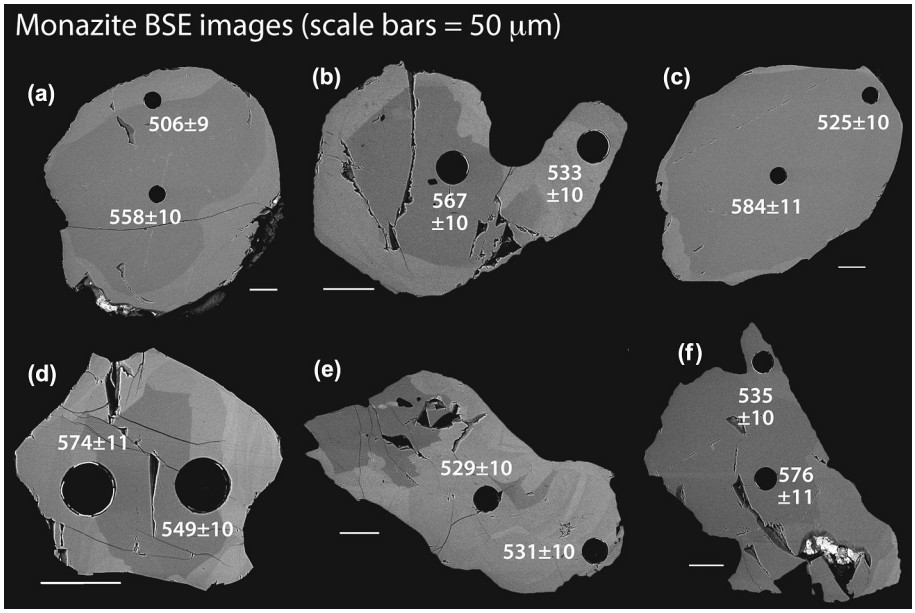

Figure 5. Back-scattered electron imaging of selected monazite grains illustrating the range in morphologies. The SHRIMP $^{206}Pb/^{238}U$ ages with associated errors (1σ) are given. Full analytical results are given in Table 3.

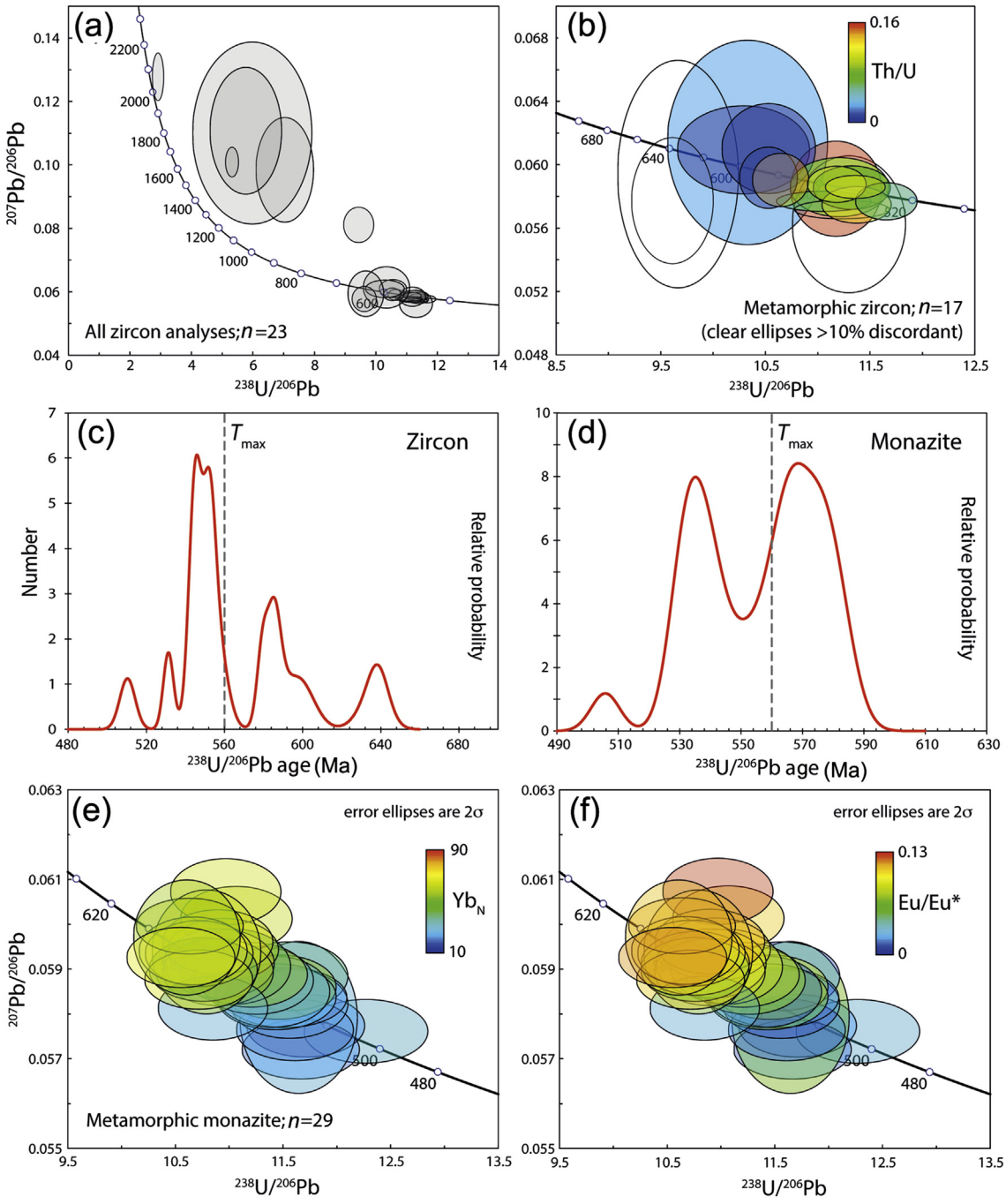

Figure 6. U–Pb geochronological data from sample I12–005a. (a) Tera-Wasserburg concordia plot showing all zircon analyses. (b) Tera-Wasserburg concordia plot for metamorphic zircon (i.e. excluding oscillatory-zoned magmatic cores) colour coded for Th/U ratio. (c) Probability-density plot for metamorphic zircon. The onset of growth of new dark CL-response metamorphic zircon began at around 560 Ma. (d) Probability-density plot for monazite showing two distinct age peaks at around 570 and 535 Ma interpreted to represent monazite growth both predating and post-dating the metamorphic peak. (e) Tera-Wasserburg concordia plot for monazite colour coded for Yb. Two distinct groups are recognised that correspond to the age peaks shown in (d), an older higher Yb (HREE) group and a younger lower Yb group. (f) Tera-Wasserburg concordia plot for monazite colour coded for Eu anomaly. Two groups are recognised, an older group with higher Eu/Eu* group and a younger group with lower Eu/Eu*.

path shown on Fig. 3 are similar to those inferred from other regions within southern India (Brown and Raith, 1996; Raith et al., 1997; Nandakumar and Harley, 2000; Sajeev et al., 2001, 2004; Braun and Appel, 2006; Ishii et al., 2006; Prakash et al., 2007; Shimizu et al., 2009; Brandt et al., 2011; Collins et al., 2014) and broadly consistent with the metamorphic evolution of the Nagercoil Block proposed by Santosh et al. (2003).

6.2. Temporal constraints

The morphology of zircon grains in sample I12–005a suggests that most grew during high-grade metamorphism, although a number of grains preserve cores inherited from the igneous rocks from which the sedimentary protoliths were in part sourced (Fig. 4). Development of sector zoning overprinting and replacing

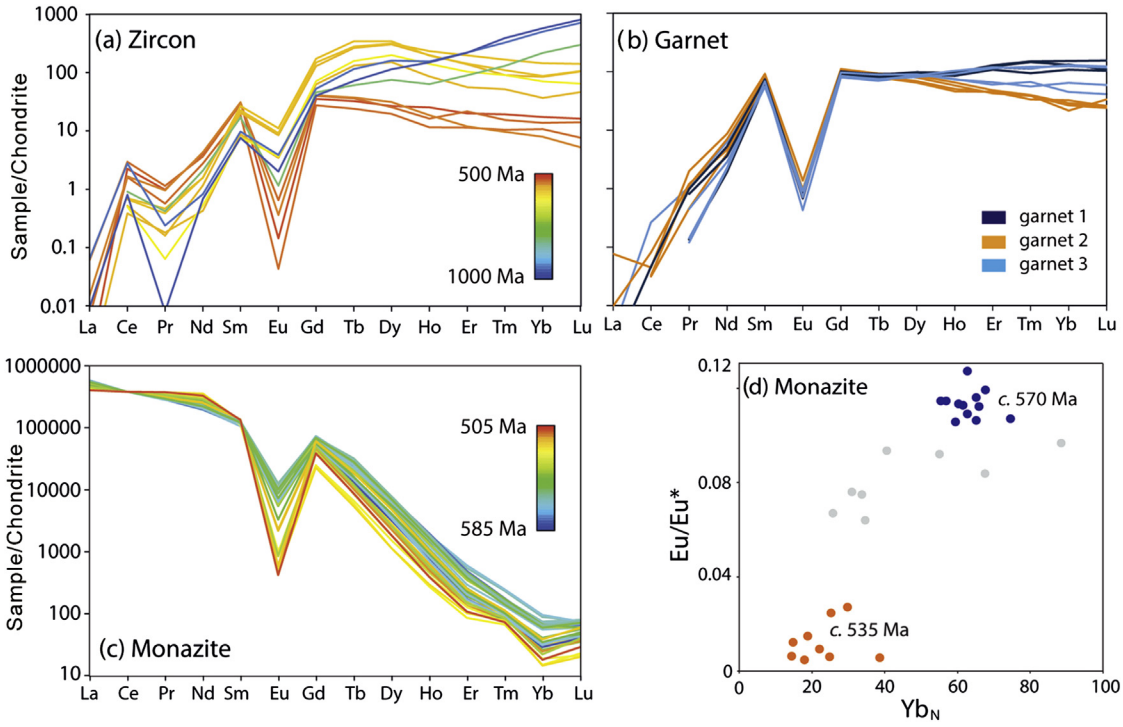

Figure 7. Chondrite-normalised REE concentration of (a) zircon, (b) garnet and (c) monazite. In (c) the data is calibrated against Ce content, which consequently shows no variation. The data for zircon and monazite are colour coded for age. (d) Yb_N vs. Eu/Eu* in monazite. Two compositionally distinct groups are identified that correspond to the two mean age peaks at around 570 and 535 Ma.

typical oscillatory-zoned igneous cores is consistent with the U–Pb data and indicates extensive isotopic resetting. These data project back along a discordia to an age of around 2000–2100 Ma (Fig. 6a) that, although poorly constrained, is interpreted as the age of the granitoid source rocks. Our data are consistent with the results reported in a recent study by Kröner et al. (2015) where widespread Palaeoproterozoic magmatic protoliths are identified in the Nagercoil and Trivandrum blocks.

The inferred metamorphic U–Pb age data from both zircon and monazite require careful interpretation, with both accessory phases showing a range in age and chemistry that suggest a complex and protracted metamorphic history. In some cases distinct age populations are identified, whereas in other cases the data overlap and/or exhibit more gradational changes that probably represent partial recrystallization and isotopic resetting. Metamorphic zircon ages range from 639 ± 10 to 531 ± 5 Ma and monazite ages range from 584 ± 11 to 506 ± 9 Ma (Fig. 6), data that together describe a long-lived high-grade metamorphic history.

Although the 2σ errors overlap with concordia, the data from the oldest sector-zoned metamorphic zircons (639–635 Ma) are imprecise and yield mean ages that are >10% inversely discordant (Fig. 6b). The oldest concordant metamorphic analyses comprise a population of five grains that together give a weighted mean $^{206}Pb/^{238}U$ age of 585 ± 10 Ma (MSWD = 2.2). This age may represent recrystallisation and partial U–Pb resetting of inherited zircon. The earlier generation of metamorphic zircon is relatively depleted in U but enriched in middle to heavy REE (Fig. 7a). When compared with garnet 1 and the core of garnet 3 (Fig. 7b), this group shows $D_{Tm\text{-}Lu}$(zircon/garnet) of close to unity, suggesting that the earliest population of metamorphic zircon was growing with garnet in the rock (e.g. Harley et al., 2001; Hokada and Harley, 2004; Kelly and Harley, 2005), consistent with the high *T* prograde segment of the *P*–*T* path shown in Fig. 3. However, the MREE are strongly partitioned into zircon, which may have been the result of these grains having formed via recrystallization of pre-existing zircon rather than by new growth. The first phase of monazite growth, characterised by low Th/U and relatively high Eu/Eu* and Yb values (Figs. 6c,d and 7c,d) gives a mean age of 572 ± 5 Ma (n = 12; MSWD = 2.5). Similar monazite ages have been reported from the crustal blocks of southern India (e.g. Braun et al., 1998; Santosh et al., 2006a; Taylor et al., 2014) and are here interpreted to record prograde growth during high-grade metamorphism (see following section).

The distinctive dark CL response zones on zircon (Fig. 4c, g–i) form broad, featureless overgrowths that are interpreted to have resulted from new growth during cooling from the metamorphic peak due decreasing solubility of Zr in melt during melt crystallisation (e.g. Kelsey et al., 2008). This interpretation is supported by the more pronounced negative Eu anomaly, which suggests this zircon was growing with plagioclase as melt crystallised (e.g. Bédard, 2006). The dark CL zones have a weighted mean $^{206}Pb/^{238}U$ age of 542 ± 8 Ma (n = 7), although the high MSWD (6.7) indicates these data are unlikely to represent a single crystallisation age. We suggest that the spread of concordant age data are geologically meaningful and record protracted growth of zircon during slow cooling and melt crystallization (Korhonen et al., 2011). Thus, the oldest concordant age of the dark CL overgrowths, at around 560 Ma, is interpreted to record the onset of melt crystallization and represents the minimum age of the metamorphic peak.

Although the later (lower HREE) garnets (garnet 2 and garnet 3 rims) also have lower middle to heavy REE concentrations, consistent D_{REE} (zircon/garnet) values of ~0.3–0.4 for the middle to heavy REE, they are unlikely to represent equilibrium growth of these two phases based on previous studies (e.g. Harley et al., 2001; Hokada and Harley, 2004; Kelly and Harley, 2005; Rubatto and Hermann, 2007; Taylor et al., 2015). It is likely that those values, which are low compared to high-*T* equilibrium values [D_{REE}(zircon/garnet) ~1], were the result of slow release of HREE during garnet breakdown during high *T* retrograde decompression, which resulted in relatively depleted zircon HREE concentrations (Fig. 7a).

The youngest ages from the sample come from high BSE response zones within monazite that cut across older, lower BSE response monazite (Fig. 4j,k). These areas, with a weighted mean $^{206}Pb/^{238}U$ age of 535 ± 4 Ma ($n = 7$; MSWD = 0.83), are interpreted to represent monazite growth during melt crystallisation while garnet was dissolving but still stable. This is supported by the pronounced negative Eu anomaly, which suggests co-crystallisation of this monazite with plagioclase, and relatively depleted HREE contents compared with earlier monazite growth (Fig. 7c).

6.3. Prograde and retrograde monazite growth?

If the estimate on the age of the metamorphic peak at around 560 Ma is correct, this implies monazite growth during both the prograde and retrograde evolution of the rocks (i.e. during both melt formation and melt recrystallization). Although monazite may grow along the prograde path in metapelites metamorphosed to (subsolidus) amphibolite conditions (e.g. Wing et al., 2003), it will begin to dissolve as the rocks melt (Rapp and Watson, 1986). Phase equilibria modelling suggests dissolution of all monazite at temperatures of around 800 °C or less, even for extreme contents of LREE (500 ppm; Yakymchuk and Brown, 2014), although such modelling cannot currently incorporate P. Experiments demonstrate that the dissolution of apatite in peraluminous melts is strongly dependent on the aluminium saturation index [ASI = molar $Al_2O_3/(CaO + Na_2O + K_2O)$] of the melt, in which the solubility of apatite increases by an order of magnitude as the ASI of the melt increases from around 1.1 to 1.2 (Wolf and London, 1994). However, the melt is unable to carry any significant quantities of REE regardless of ASI (Wolf and London, 1995). The result is that, during partial melting in which the ASI of the melt is increasing, REE-rich apatite should break down incongruently to form REE-rich monazite and REE-depleted melt (Wolf and London, 1995).

Fig. 8 shows the calculated ASI of the melt produced along a simplified isobaric (7 kbar) heating path from 810 to 950 °C, a first-order approximation to the high–T portion of the example P–T shown on Fig. 2. Across this interval the ASI of the melt increases from 1.16 to 1.27. Apatite is likely to have been the main REE carrying phase within the aluminous metapelite sample I12–005a at lower grades. Apatite would have broken down with increasing temperature to form REE-enriched monazite, consistent with the low BSE response monazite cores in sample I12–005a (Figs. 4j–l and 7c). As the melt began to crystallise, any remaining P_2O_5 dissolved in the melt would have crystallised to form relatively REE-depleted monazite, consistent with the higher BSE response monazite rims (Figs. 4j–l and 7c). The small enrichment in Ca in the older monazite is consistent with the interpretation that the earlier generation grew by the incongruent breakdown of apatite.

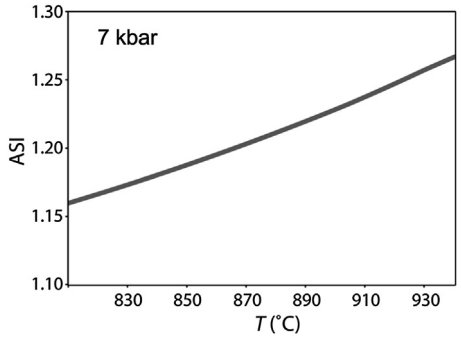

Figure 8. Calculated aluminium saturation index [ASI = molar $Al_2O_3/(CaO + Na_2O + K_2O)$] of the melt produced with heating along a prograde path at 7 kbar. Experiments show the solubility of apatite increases by an order of magnitude as the ASI increases from around 1.1 to 1.2 (Wolf and London, 1994).

6.4. Regional context

Clockwise P–T paths similar to those constrained here for the Nagercoil Block and for other regions within the Southern Granulite Terrane in India have been interpreted to be the result of protracted Ediacaran–Cambrian orogenesis as Neoproterozoic India collided with Azania–East Africa in a setting similar to modern day Tibet (Hacker et al., 2000; Collins and Pisarevsky, 2005; Collins et al., 2014). The crustal oxygen isotope values and the absence of any significant volumes of mafic/ultramafic rocks suggest that the heat required for the ultrahigh-temperature metamorphism was derived largely from thickened crust with elevated concentrations of radiogenic heat-producing elements (Clark et al., 2011, 2014) rather than from significant mantle-derived melt advection.

The Nagercoil Block is interpreted to be exotic, lying to the south and east of the southern boundary of Neoproterozoic India, the Palghat-Cauvery shear system (Collins et al., 2007a,b; Plavsa et al., 2014; Fig. 1). It is also inferred to lie south of the southern margin of Azania, the Neoproterozoic belt defined by the southern Madurai Block and Achankovil Belt (Tomson et al., 2013; Collins et al., 2014; Plavsa et al., 2014). In these highly deformed and metamorphosed rocks, pre-collisional and orogenic polarity is hard to determine. Neoproterozoic metaigneous rocks in the Madurai Block that have been interpreted to lie above a subduction zone (Teale et al., 2011; Plavsa et al., 2012) were correlated with Cryogenian continental-arc rocks in central Madagascar (Handke et al., 1999; Plavsa et al., 2012) to suggest that Azania formed the upper plate in the Azania/Neoproterozoic India collision. Whether the collision of the Nagercoil Block (with or without the Trivandrum Block) with Azania had a polarity sympathetic to this is unknown, but the absence of Neoproterozoic magmatic protoliths in the Nagercoil Block suggests that the Nagercoil Block may have formed the lower plate of this collision zone.

The pre-Gondwana affinity of the Nagercoil Block is the subject of considerable conjecture. U–Pb and Hf isotopic data from zircon (Clark et al., unpublished) suggests that the dominant igneous charnockites are similar to the SE Congo–Tanzania–Bangweulu Block of Africa and therefore the ultimate origin of the Nagercoil Block was as part of this terrane. A second possibility is that the Nagercoil Block correlates with the Androyen domain of southern Madagascar, where similar-aged protoliths have been reported (Tucker et al., 2014). Boger et al. (2014) suggest that this terrane may have formed a Neoproterozoic microcontinent separate from Azania, Neoproterozoic India and the Congo–Tanzania–Bangweulu Block.

Data from Clark et al. (unpublished) suggest that the Nagercoil Block has a different tectonic affinity to the other blocks that make up the Southern Granulite Terrane. In the previous sections we demonstrated that the timing and conditions of metamorphism were near identical with those experienced by these other crustal blocks, consistent with the observation that it was the terminal suturing of Gondwana that led to the final relationships of these blocks. Post Gondwana breakup, the Nagercoil Block remained attached to India rather than Africa.

Acknowledgements

Funding for analyses and fieldwork was provided through Australian Research Council (ARC) Discovery and DECRA projects DP0879330 and DE1201030 (to CC), Future Fellowship Scheme #FT120100340 (to ASC) and the Australia-India Strategic Research Fund project #ST030046 (to CC and ASC). CC and RT acknowledge support from Curtin University Strategic Research Funding. Zircon and monazite U–Pb analyses were carried out using the SHRIMP-II Ion Microprobe at the John de Laeter Centre for Isotope Research, Perth, managed by Allen Kennedy on behalf of a consortium

consisting of Curtin University, the Geological Survey of Western Australia, and the University of Western Australia with the support of the ARC. REE analyses were carried out at the LA–ICP–MS Facility at the Department of Applied Geology, Curtin University. We are grateful to Brad Hacker, Qiong-Yan Yang and an anonymous reviewer for comments that led to an improvement in the final version, to Simon Harley for his advice, and to S. Kwon for his proficient editorial handling. Any remaining infelicities are ours. ASC's contribution forms TRaX Record #323. This is contribution 526 from the ARC Centre of Excellence for Core to Crust Fluid Systems (http://www.ccfs.mq.edu.au).

Appendix A. Supplementary data

Supplementary data related to this article can be found at http://dx.doi.org/10.1016/j.gsf.2014.12.003.

References

Bédard, J.H., 2006. Trace element partitioning in plagioclase feldspar. Geochimica et Cosmochimica Acta 70, 3717–3742.
Bogdanova, S.V., Li, Z.X., Moores, E.M., Pisarevsky, S.A., 2008. Testing the Rodinia hypothesis: records in its building blocks. Precambrian Research 160, 1–4.
Boger, S.D., Miller, J.M., 2004. Terminal suturing of Gondwana and the onset of the Ross-Delamerian Orogeny: the cause and effect of an Early Cambrian reconfiguration of plate motions. Earth and Planetary Science Letters 219, 35–48.
Boger, S.D., Hirdes, W., Ferreira, C.A.M., Jenett, T., Dallwig, R., Fanning, C.M., 2014. The 580–520 Ma Gondwana suture of Madagascar and its continuation into Antarctica and Africa. Gondwana Research. http://dx.doi.org/10.1016/j.gr.2014.08.017.
Brandt, S., Schenk, V., Raith, M.M., Appel, P., Gerdes, A., Srikantappa, C., 2011. Late neoproterozoic P-T evolution of HP-UHT granulites from the palni hills (South India): new constraints from phase diagram modelling, LA-ICP-MS zircon dating and in-situ EMP monazite dating. Journal of Petrology 52, 1813–1856.
Braun, I., Montel, J.M., Nicollet, C., 1998. Electron microprobe dating of monazites from high-grade gneisses and pegmatites of the Kerala Khondalite Belt, southern India. Chemical Geology 146, 65–85.
Braun, I., Appel, P., 2006. U-Th-total Pb dating of monazite from orthogneisses and their ultra-high temperature metapelitic enclaves: Implications for the multi-stage tectonic evolution of the Madurai Block, southern India. European Journal of Mineralogy 18, 415–427.
Brown, M., Raith, M., 1996. First evidence of ultrahigh-temperature decompression from the granulite province of southern India. Journal of the Geological Society 153, 819–822.
Brown, M., 2014. The contribution of metamorphic petrology to understanding lithosphere evolution and geodynamics. Geoscience Frontiers 5, 553–569.
Buick, I.S., Clark, C., Rubatto, D., Hermann, J., Pandit, M., Hand, M., 2010. Constraints on the Proterozoic evolution of the Aravalli-Delhi Orogenic belt (NW India) from monazite geochronology and mineral trace element geochemistry. Lithos 120, 511–528.
Cenki, B., Braun, I., Bröcker, M., 2004. Evolution of the continental crust in the Kerala Khondalite Belt, southernmost India: evidence from Nd isotope mapping, U-Pb and Rb-Sr geochronology. Precambrian Research 134, 275–292.
Clark, C., Collins, A.S., Santosh, M., Taylor, R., Wade, B.P., 2009a. The *P–T–t* architecture of a Gondwanan suture: REE, U-Pb and Ti-in-zircon thermometric constraints from the Palghat Cauvery shear system, South India. Precambrian Research 174, 129–144.
Clark, C., Collins, A.S., Timms, N.E., Kinny, P.D., Chetty, T.R.K., Santosh, M., 2009b. SHRIMP U-Pb age constraints on magmatism and high-grade metamorphism in the Salem Block, southern India. Gondwana Research 16, 27–36.
Clark, C., Fitzsimons, I.C.W., Healy, D., Harley, S.L., 2011. How does the continental crust get really hot? Elements 7, 235–240.
Clark, C., Healy, D., Johnson, T.E., Collins, A.S., Taylor, R.J., Santosh, M., 2014. Hot orogens and supercontinent amalgamation: a Gondwanan example using SHRIMP U-Pb geochronology, REE geochemistry, phase equilibria and numerical modelling. Gondwana Research. http://dx.doi.org/10.1016/j.gr.2014.11.005.
Collins, A.S., Pisarevsky, S.A., 2005. Amalgamating eastern Gondwana: the evolution of the Circum-Indian orogens. Earth-Science Reviews 71, 229–270.
Collins, A.S., Clark, C., Sajeev, K., Santosh, M., Kelsey, D.E., Hand, M., 2007a. Passage through India: the Mozambique Ocean suture, high-pressure granulites and the Palghat-Cauvery shear zone system. Terra Nova 19, 141–147.
Collins, A.S., Santosh, M., Braun, I., Clark, C., 2007b. Age and sedimentary provenance of the Southern Granulites, South India. U-Th-Pb SHRIMP secondary ion mass spectrometry. Precambrian Research 155, 125–138.
Collins, A.S., Clark, C., Plavsa, D., 2014. Peninsular India in Gondwana: the tectonothermal evolution of the Southern Granulite Terrain and its Gondwanan counterparts. Gondwana Research 25, 190–203.
Corfu, F., Hanchar, J.M., Hoskin, P.W.O., Kinny, P., 2003. Atlas of zircon textures. Reviews in Mineralogy and Geochemistry 53, 469–500.
Diener, J.F.A., Powell, R., White, R.W., 2008. Quantitative phase petrology of cordierite-orthoamphibole gneisses and related rocks. Journal of Metamorphic Geology 26, 795–814.
Evans, K.A., Bickle, M.J., 2005. An investigation of the relationship between bulk composition, inferred reaction progress and fluid-flow parameters for layered micaceous carbonates from Maine, USA. Journal of Metamorphic Geology 23, 181–197.
Ghosh, J.G., de Wit, M.J., Zartman, R.E., 2004. Age and tectonic evolution of Neoproterozoic ductile shear zones in the Southern Granulite Terrain of India, with implications for Gondwana studies. Tectonics 23, 3001–3038. TC3006.
Hacker, B.R., Gnos, E., Ratschbacher, L., Grove, M., McWilliams, M., Sobolev, S.V., Wan, J., Wu, Z., 2000. Hot and dry deep crustal xenoliths from Tibet. Science 287, 2463–2466.
Handke, M.J., Tucker, R.D., Ashwal, L.D., 1999. Neoproterozoic continental arc magmatism in west-central Madagascar. Geology 27, 351–354.
Harley, S.L., 1998. On the occurrence and characterization of ultrahigh-temperature crustal metamorphism. Geological Society Special Publication, pp. 81–107.
Harley, S.L., Kinny, P., Snape, I., Black, L.P., 2001. Zircon chemistry and the definition of events in Archean granulite terrains. In: Fourth International Archean Symposium, Extended Abstract Volume, pp. 511–513. AGSO Geoscience Australia Record 2001/37.
Harley, S.L., Kelly, N.M., Möller, A., 2007. Zircon behaviour and the thermal histories of mountain chains. Elements 3, 25–30.
Hermann, J., Rubatto, D., 2003. Relating zircon and monazite domains to garnet growth zones: age and duration of granulite facies metamorphism in the Val Malenco lower crust. Journal of Metamorphic Geology 21, 833–852.
Hokada, T., Harley, S.L., 2004. Zircon growth in UHT leucosome: constraints from zircon-garnet rare earth elements (REE) relations in Napier Complex, East Antarctica. Journal of Mineralogical and Petrological Sciences 99, 180–190.
Holland, T.J.B., Powell, R., 2011. An improved and extended internally consistent thermodynamic dataset for phases of petrological interest, involving a new equation of state for solids. Journal of Metamorphic Geology 29, 333–383.
Hoskin, P.W.O., Black, L.P., 2000. Metamorphic zircon formation by solid-state recrystallization of protolith igneous zircon. Journal of Metamorphic Geology 18, 423–439.
Ishii, S., Tsunogae, T., Santosh, M., 2006. Ultrahigh-temperature metamorphism in the Achankovil Zone: implications for the correlation of crustal blocks in southern India. Gondwana Research 10, 99–114.
Johnson, T., Brown, M., 2004. Quantitative constraints on metamorphism in the Variscides of southern Brittany – A complementary pseudosection approach. Journal of Petrology 45, 1237–1259.
Johnson, T.E., White, R.W., Powell, R., 2008. Partial melting of metagreywacke: a calculated mineral equilibria study. Journal of Metamorphic Geology 26, 837–853.
Johnson, T.E., Brown, M., White, R.W., 2010. Petrogenetic modelling of strongly residual metapelitic xenoliths within the southern Platreef, Bushveld Complex, South Africa. Journal of Metamorphic Geology 28, 269–291.
Johnson, T.E., White, R.W., 2011. Phase equilibrium constraints on conditions of granulite-facies metamorphism at Scourie, NW Scotland. Journal of the Geological Society 168, 147–158.
Johnson, T.E., Brown, M., Kaus, B., VanTongeren, J.A., 2014. Delamination and recycling of Archaean crust caused by gravitational instabilities. Nature Geoscience 7, 47–52.
Kelly, N.M., Harley, S.L., 2005. An integrated microtextural and chemical approach to zircon geochronology: refining the Archaean history of the Napier Complex, east Antarctica. Contributions to Mineralogy and Petrology 149, 57–84.
Kelsey, D.E., 2008. On ultrahigh-temperature crustal metamorphism. Gondwana Research 13, 1–29.
Kelsey, D.E., Clark, C., Hand, M., 2008. Thermobarometric modelling of zircon and monazite growth in melt-bearing systems: examples using model metapelitic and metapsammitic granulites. Journal of Metamorphic Geology 26, 199–212.
Kelsey, D.E., Powell, R., 2011. Progress in linking accessory mineral growth and breakdown to major mineral evolution in metamorphic rocks: a thermodynamic approach in the Na_2O-CaO-K_2O-FeO-MgO-Al_2O_3-SiO_2-H_2O-TiO_2-ZrO_2 system. Journal of Metamorphic Geology 29, 151–166.
Kelsey, D.E., Hand, M., 2015. On ultrahigh temperature crustal metamorphism: phase equilibria, trace element thermometry, bulk composition, heat sources, timescales and tectonic settings. Geoscience Frontiers, 6, 311–356.
Korhonen, F.J., Saw, A.K., Clark, C., Brown, M., Bhattacharya, S., 2011. New constraints on UHT metamorphism in the Eastern Ghats Province through the application of phase equilibria modelling and in situ geochronology. Gondwana Research 20, 764–781.
Korhonen, F.J., Brown, M., Clark, C., Bhattacharya, S., 2013. Osumilite-melt interactions in ultrahigh temperature granulites: phase equilibria modelling and implications for the *P–T–t* evolution of the Eastern Ghats Province, India. Journal of Metamorphic Geology 31, 881–907.
Korhonen, F.J., Clark, C., Brown, M., Taylor, R.J.M., 2014. Taking the temperature of Earth's hottest crust. Earth and Planetary Science Letters 408, 341–353.
Kröner, A., 1984. Evolution, growth and stabilization of the Precambrian lithosphere. Physics and Chemistry of the Earth 15, 69–106.
Kröner, A., Santosh, M., Wong, J., 2012. Zircon ages and Hf isotopic systematics reveal vestiges of Mesoproterozoic to Archaean crust within the late Neoproterozoic-Cambrian high-grade terrain of southernmost India. Gondwana Research 21, 876–886.

Kröner, A., Santosh, M., Hegner, E., Shaji, E., Geng, H., Wong, J., Xie, H., Wan, Y., Shang, C.K., Liu, D., Sun, M., Nanda-Kumar, V., 2015. Palaeoproterozoic ancestry of Pan-African high-grade granitoids in southernmost India: Implications for Gondwana reconstructions. Gondwana Research 27, 1–37.
Meert, J.G., 2003. A synopsis of events related to the assembly of the eastern Gondwana. Tectonophysics 362, 1–40.
Meert, J.G., Lieberman, B.S., 2008. The Neoproterozoic assembly of Gondwana and its relationship to the Ediacaran–Cambrian radiation. Gondwana research 14, 5–21.
Mezger, K., Krogstad, E.J., 1997. Interpretation of discordant U-Pb zircon ages: an evaluation. Journal of Metamorphic Geology 15, 127–140.
Nance, R.D., Murphy, J.B., Santosh, M., 2014. The supercontinent cycle: a retrospective essay. Gondwana Research 25, 4–29.
Nandakumar, V., Harley, S.L., 2000. A reappraisal of the pressure-temperature path of granulites from the Kerala Khondalite Belt, Southern India. Journal of Geology 108, 687–703.
Pisarevsky, S.A., Murphy, J.B., Cawood, P.A., Collins, A.S., 2008. Late Neoproterozoic and Early Cambrian Palaeogeography: Models and Problems. Geological Society Special Publication, pp. 9–31.
Plavsa, D., Collins, A.S., Foden, J.F., Kropinski, L., Santosh, M., Chetty, T.R.K., Clark, C., 2012. Delineating crustal domains in Peninsular India: age and chemistry of orthopyroxene-bearing felsic gneisses in the Madurai Block. Precambrian Research 198–199, 77–93.
Plavsa, D., Collins, A.S., Payne, J.L., Foden, J.D., Clark, C., Santosh, M., 2014. Detrital zircons in basement metasedimentary protoliths unveil the origins of southern India. Bulletin of the Geological Society of America 126, 791–812.
Powell, R., Holland, T.J.B., 1988. An internally consistent dataset with uncertainties and correlations: 3. Applications to geobarometry, worked examples and a computer program. Journal of Metamorphic Geology 6, 173–204.
Powell, C.M., Pisarevsky, S.A., 2002. Late neoproterozoic assembly of East Gondwana. Geology 30, 3–6.
Prakash, D., Arima, M., Mohan, A., 2007. Ultrahigh-temperature mafic granulites from Panrimalai, south India: constraints from phase equilibria and thermobarometry. Journal of Asian Earth Sciences 29, 41–61.
Raith, M., Karmakar, S., Brown, M., 1997. Ultra-high-temperature metamorphism and multistage decompressional evolution of sapphirine granulites from the Palni Hill Ranges, southern India. Journal of Metamorphic Geology 15, 379–399.
Rajesh, H.M., Santosh, M., Yoshikura, S., 2011. The Nagercoil charnockite: a magnesian, calcic to calc-alkalic granitoid dehydrated during a granulite-facies metamorphic event. Journal of Petrology 52, 375–400.
Rajesh, H.M., Santosh, M., 2012. Charnockites and charnockites. Geoscience Frontiers 3, 737–744.
Rapp, R.P., Watson, E.B., 1986. Monazite solubility and dissolution kinetics – implications for the thorium and light rare-earth chemistry of felsic magmas. Contributions to Mineralogy and Petrology 94, 304–316.
Rebay, G., Powell, R., Diener, J.F.A., 2010. Calculated phase equilibria for a morb composition in a P-T range, 450-650 °C and 18-28 kbar: the stability of eclogite. Journal of Metamorphic Geology 28, 635–645.
Rubatto, D., 2002. Zircon trace element geochemistry: Partitioning with garnet and the link between U-Pb ages and metamorphism. Chemical Geology 184, 123–138.
Rubatto, D., Hermann, J., Buick, I.S., 2006. Temperature and bulk composition control on the growth of monazite and zircon during low-pressure anatexis (Mount Stafford, Central Australia). Journal of Petrology 47, 1973–1996.
Rubatto, D., Hermann, J., 2007. Experimental zircon/melt and zircon/garnet trace element partitioning and implications for the geochronology of crustal rocks. Chemical Geology 241, 38–61.
Sajeev, K., Osanai, Y., Santosh, M., 2001. Ultrahigh-temperature stability of Sapphirine and Kornerupine in Ganguvarpatti Granulite, Madurai Block, Southern India. Gondwana Research 4, 762–766.
Sajeev, K., Osanai, Y., Santosh, M., 2004. Ultrahigh-temperature metamorphism followed by two-stage decompression of garnet-orthopyroxene-sillimanite granulites from Ganguvarpatti, Madurai block, southern India. Contributions to Mineralogy and Petrology 148, 29–46.
Santosh, M., 1996. The Trivandrum and Nagercoil Granulite Blocks. Gondwana Research Group Memoir 3, pp. 243–277.
Santosh, M., Tagawa, M., Taguchi, S., Yoshikura, S., 2003. The Nagercoil Granulite Block, southern India: petrology, fluid inclusions and exhumation history. Journal of Asian Earth Sciences 22, 131–155.
Santosh, M., Morimoto, T., Tsutsumi, Y., 2006a. Geochronology of the khondalite belt of Trivandrum Block, Southern India: electron probe ages and implications for Gondwana tectonics. Gondwana Research 9, 261–278.
Santosh, M., Tagawa, M., Yokoyama, K., Collins, A.S., 2006b. U-Pb electron probe geochronology of the Nagercoil granulites, Southern India: implications for Gondwana amalgamation. Journal of Asian Earth Sciences 28, 63–80.
Santosh, M., Maruyama, S., Sato, K., 2009. Anatomy of a Cambrian suture in Gondwana: Pacific-type orogeny in southern India? Gondwana Research 16, 321–341.
Scotese, C.R., 2009. Late Proterozoic Plate Tectonics and Palaeogeography: a Tale of Two Supercontinents, Rodinia and Pannotia. Geological Society Special Publication, pp. 67–83.
Shimizu, H., Tsunogae, T., Santosh, M., 2009. Spinel + quartz assemblage in granulites from the Achankovil Shear Zone, southern India: implications for ultrahigh-temperature metamorphism. Journal of Asian Earth Sciences 36, 209–222.
Taylor, R.J.M., Clark, C., Fitzsimons, I.C.W., Santosh, M., Hand, M., Evans, N., McDonald, B., 2014. Post-peak, fluid-mediated modification of granulite facies zircon and monazite in the Trivandrum Block, southern India. Contributions to Mineralogy and Petrology 168.
Taylor, R.J.M., Harley, S.L., Hinton, R.W., Elphick, S., Clark, C., Kelly, N.M., 2015. Experimental determination of REE partition coefficients between zircon, garnet and melt: a key to understanding high-temperature crustal processes. Journal of Metamorphic Geology 33 (3), 231–248.
Teale, W., Collins, A.S., Foden, J., Payne, J.L., Plavsa, D., Chetty, T.R.K., Santosh, M., Fanning, M., 2011. Cryogenian (~830Ma) mafic magmatism and metamorphism in the northern Madurai Block, southern India: a magmatic link between Sri Lanka and Madagascar? Journal of Asian Earth Sciences 42, 223–233.
Tomson, J.K., Bhaskar Rao, Y.J., Vijaya Kumar, T., Choudhary, A.K., 2013. Geochemistry and neodymium model ages of Precambrian charnockites, Southern Granulite Terrain, India: constraints on terrain assembly. Precambrian Research 227, 295–315.
Torsvik, T.H., Carter, L.M., Ashwal, L.D., Bhushan, S.K., Pandit, M.K., Jamtveit, B., 2001. Rodinia refined or obscured: palaeomagnetism of the Malani igneous suite (NW India). Precambrian Research 108, 319–333.
Trindade, R.I.F., D'Agrella-Filho, M.S., Epof, I., Brito Neves, B.B., 2006. Paleomagnetism of Early Cambrian Itabaiana mafic dikes (NE Brazil) and the final assembly of Gondwana. Earth and Planetary Science Letters 244, 361–377.
Trompette, R., 1997. Neoproterozoic (~600 Ma) aggregation of Western Gondwana: a tentative scenario. Precambrian Research 82, 101–112.
Tucker, R.D., Roig, J.Y., Moine, B., Delor, C., Peters, S.G., 2014. A geological synthesis of the Precambrian shield in Madagascar. Journal of African Earth Sciences 94, 9–30.
White, R.W., Powell, R., Holland, T.J.B., 2001. Calculation of partial melting equilibria in the system. Journal of Metamorphic Geology 19, 139–153.
White, R.W., Powell, R., 2002. Melt loss and the preservation of granulite facies mineral assemblages. Journal of Metamorphic Geology 20, 621–632.
White, R.W., Powell, R., Holland, T.J.B., 2007. Progress relating to calculation of partial melting equilibria for metapelites. Journal of Metamorphic Geology 25, 511–527.
White, R.W., Powell, R., Holland, T.J.B., Johnson, T.E., Green, E.C.R., 2014a. New mineral activity-composition relations for thermodynamic calculations in metapelitic systems. Journal of Metamorphic Geology 32, 261–286.
White, R.W., Powell, R., Johnson, T.E., 2014b. The effect of Mn on mineral stability in metapelites revisited: new *a-x* relations for manganese-bearing minerals. Journal of Metamorphic Geology 32, 809–828.
Wing, B.A., Ferry, J.M., Harrison, T.M., 2003. Prograde destruction and formation of monazite and allanite during contact and regional metamorphism of pelites: petrology and geochronology. Contributions to Mineralogy and petrology 145, 228–250.
Wolf, M.B., London, D., 1994. Apatite dissolution into peraluminous haplogranitic melts: an experimental study of solubilities and mechanisms. Geochimica et Cosmochimica Acta 58, 4127–4145.
Wolf, M.B., London, D., 1995. Incongruent dissolution of REE- and Sr-rich apatite in peraluminous granitic liquids: differential apatite, monazite, and xenotime solubilities during anatexis. American Mineralogist 80, 765–775.
Yakymchuk, C., Brown, M., 2014. Behaviour of zircon and monazite during crustal melting. Journal of the Geological Society 171, 465–479.

Tim Johnson is a lecturer at Curtin University in Western Australia. His research concentrates on crystalline rocks and what these can tell us about fundamental lithospheric processes. His expertise is in metamorphic petrology, in particular the application of phase equilibria modelling and the generation, segregation and migration of melt in the crust and upper mantle. More recently his research has concentrated on Archaean geodynamics and the generation and modification of Earth's first crust.

Chris Clark is a principal research fellow in metamorphic geology and geochronology at Curtin University in Western Australia. His main research interests are in the linking of geochronology, specifically the U–Pb method using zircon and monazite, with the development of metamorphic assemblages in order to constrain the durations of mountain-building events in high-grade metamorphic terranes.

Rich Taylor is a research associate at Curtin University in Western Australia. His expertise lie primarily in the fields of experimental petrology and analytical geochemistry, particularly related to high-grade metamorphism. He uses multi-instrument techniques to evaluate geological processes based on trace element and isotopic compositions of major and accessory phases.

M. Santosh is Professor at the China University of Geosciences Beijing (China), Specially Appointed Foreign Expert of China, and Emeritus Professor at the Faculty of Science, Kochi University, Japan. He obtained his B.Sc. (1978) from Kerala University, his M.Sc. (1981) from the University of Roorkee, his Ph.D. (1986) from Cochin University of Science and Technology, a D.Sc. (1990) from Osaka City University and another (2012) from the University of Pretoria. He is the Founding Editor of Gondwana Research and the founding Secretary General of the International Association for Gondwana Research. His research fields include petrology, fluid inclusions, geochemistry, geochronology and supercontinent tectonics. He has published over 350 research papers, edited several memoir volumes and journal special issues, and is co-author of the book 'Continents and Supercontinents' (Oxford University Press, 2004). He has been the recipient of a National Mineral Award, an Outstanding Geologist Award, a Thomson Reuters 2012 Research Front Award, a Global Talent Award, an Island Arc Award and a Thomson Highly Cited Top Frontier Researcher in the World award.

Prof. Alan Collins is a graduate of the Royal School of Mines, Imperial College, London and did his PhD on the multistage obduction and thrust history of the Lycian Nappes in Turkey, based at Edinburgh University, UK. From then he has worked on a variety of tectonic problems, integrating various geological disciplines to best answer tectonic problems. Alan worked in the University of Leicester, UK, Curtin University and the University of Western Australia before moving to the University of Adelaide in 2005. He is presently a professor of geology, an Australian Research Council Future Fellow and the Director of the University of Adelaide's Centre for Tectonics, Resources and Exploration (TRaX).